MOX Fuel corrosion processes under waste disposal conditions

Christophe Jegou, Melina Odorowski, Valentin Kerleguer, Véronique Broudic, Michel Schlegel, Gauthier Jouan, Caroline Marques, Laurent de Windt

MOX Fuel corrosion processes under waste disposal conditions

Christophe Jegou[1*], Melina Odorowski[1,3], Valentin Kerleguer[1,3], Véronique Broudic[1], Michel L. Schlegel[2], Gauthier Jouan[1], Caroline Marques[1], Laurent De Windt[3]

1 CEA, DES, ISEC, DE2D, University of Montpellier, Marcoule, France

2 Université Paris Saclay, CEA, Service d'Études Analytiques et de Réactivité des Surfaces, F-91191 Gif Sur Yvette, France

3 MINES ParisTech, PSL University, Centre de Géosciences, 35 rue St Honoré, F-77305 Fontainebleau, France

Keywords : MOX fuel, corrosion, geological disposal, radiolysis, iron, actinides

Abstract

The oxidative dissolution of a $(U,Pu)O_2$ MOX fuel under α radiolysis of water was studied under chemical conditions of increasing complexity in the context of the geological disposal of radioactive waste. The results show noticeable effects of a synthetic Callovian-Oxfordian claystone water and of Fe(II) on the oxidative dissolution. The presence of metallic iron in the system leads to an inhibition of the oxidative dissolution by the consumption of oxidizing species produced by water radiolysis at the MOX/water interface. The environmental effects observed with groundwater and reducing Fe(II)-species are very similar to those already observed on UO_2-based fuels.

* Corresponding author : christophe.jegou@cea.fr

Introduction

Understanding the corrosion mechanisms of irradiated fuels is a major issue for countries which have chosen the direct disposal of spent fuels in deep geological repositories. Most of the studies have been carried out so far on UO_2-based fuels to identify the alteration mechanisms and radionuclide releases under a wide range of redox conditions [1-4]. The oxydo-reduction (redox) potential is a key parameter controlling the $UO_{2(s)}$ matrix stability. Under reducing conditions such as those existing in granite or clay environments, UO_2 solubility is very low, which ensures the stability of the UO_2 fuel matrix enclosing most of the radionuclides [1]. Nevertheless, over the long term, a dominant α self-irradiation field at the fuel surface generates molecular and radical species likely to have a local impact on the redox conditions, via water radiolysis [2, 5, 6]. Oxidizing species produced by water radiolysis can especially increase the corrosion potential at the fuel/water interface, and induce an oxidative dissolution of UO_2. The overall mechanism of oxidative dissolution is generally described as a succession of steps involving oxidation of uranium at the fuel surface, dissolution of the uranyl ion and precipitation of secondary phases depending on the solution chemistry. The oxidation process occurs in two steps with a single electron transfer at each step and involves the formation of U(V) intermediate species. U(V) species can be further oxidized to U(VI) or be involved in the catalytic decomposition of oxidizing species such as hydrogen peroxide [7].

The amplitude of the oxidative dissolution depends on the strength of the α irradiation field and the redox buffering capacity of the disposal environment through the supply of reducing species [1]. The anoxic corrosion of low-alloyed steel containers containing spent fuel assemblies produces especially significant amounts of H_2 [4, 8-11]. Iron and hydrogen (H_2) reducing species can inhibit the oxidative dissolution of UO_2-based fuels [8, 12-15] and promote the retention of redox-sensitive radionuclides by stabilizing the less soluble reduced forms [10, 16].

Unlike UO_2 based fuel, little is known about the behavior of the $U_{1-x}Pu_xO_2$ Mixed OXide (MOX) fuels, and especially about the corrosion mechanisms of the heterogeneous Mimas® (**Mi**cronization of a **mas**ter blend) MOX fuel. This type of fuel, which is industrially produced after reprocessing of UO_2-based spent fuel, is used in light water nuclear reactors. Although the corrosion mechanisms are likely to be similar to those of UO_2 fuels [1], it remains essential to study the oxidative dissolution of Mimas® MOX fuel under realistic environmental conditions while also taking into account the special features of this kind of fuel.

The microstructural analysis of Mimas® MOX fuel reveals the presence of zones with different Pu contents coming from the fabrication process (dilution of a UO_2 and PuO_2 oxide blend in UO_2 powder) and from the origin of the UO_2 powder used [17]. These different Pu contents can change the

electrochemical response of the fluorite structure with respect to oxidation [18, 19]. Moreover, the average α activity of these MOX fuels is greater than that of UO_2-based fuels. The production of oxidizing species by α radiolysis of water at the solid/water interface for the same duration of radioactive decay is therefore higher. Alpha activities can also change locally depending on the local Pu content, which justifies taking the fuel heterogeneity into account in the studies [19].

Regarding the effect of environmental conditions, recent studies have confirmed that H_2 can effectively inhibit the oxidative dissolution of irradiated and unirradiated MOX fuels [18, 20]. The effects of metal iron and groundwater chemistry have been the subject of fewer investigations [21]. The goal of this study is to determine the respective effects of these environmental constraints for experimental conditions close to those expected in the French geological disposal site. According to the technical choices considered to date, each spent fuel assembly would be enclosed in a low-carbon steel overpack and placed in long horizontal cells. The preselected site is a deep clay Callovian-Oxfordian age geological formation (Cox claystone) with reducing conditions. For this experimental study, a step-by-step experimental approach gradually complexifying the environmental conditions was developed. These conditions range from carbonated water to synthetic Cox groundwater and include the presence of corroded metallic iron. Unirradiated MOX fuel pellets with a high α activity (1.3×10^9 Bq.g^{-1}) induced by α decay of Pu were used for the leaching experiments. Under the scenario of groundwater access to spent fuel after many thousands of years, α irradiation will become predominant because of the β/γ radioactive decay over the first decades [2]. Furthermore, quite high α activity enables oxidative dissolution to be amplified, and better highlights any environmental effect on the MOX fuel dissolution.

1) Materials and methods

1-1) Materials

1-1-1) Mimas® MOX fuel pellets

Unirradiated Mimas® MOX fuel pellets containing an average of 7.48 wt.% of PuO_2 were manufactured at Marcoule Melox plant (France) from Ammonium Di-Uranate type UO_2 powder. These samples have a special microstructure due to the Mimas® fabrication process in which a primary blend of UO_2 and PuO_2 is diluted with UO_2 [17]. After sintering, the final microstructure is heterogeneous and shows three main different phases:

- a UO_2 matrix containing around 2.7 hma% (heavy metal atoms) of Pu (corresponding to 15 % of total Pu),
- Pu-rich agglomerates with 20.2 hma% of Pu (40 % of total Pu),
- a coating area with an intermediate content of 7.3 hma% of Pu (45 % of total Pu).

In addition, these phases are not found in equal quantities in the fuel. The surface fractions are 46.7, 42.2 and 11.1 % for the UO_2 matrix, the coating zone and the Pu-enriched agglomerates, respectively [22]. The chemical and isotopic compositions of the MOX pellets are given in Table 1. In order to restore the stoichiometry, the polished pellets (8 mm in diameter and 2 mm thick) on one face were subjected before the leaching tests to:

- A thermal annealing at 1000 °C for 16 hours under an Ar/H_2 5%/20000 ppm H_2O atmosphere.
- About ten one-hour pre-leaching cycles (with one night for the sixth cycle) in carbonated water ($NaHCO_3$ 10^{-3}M). The goal of the pre-leaching cycles was to eliminate as much as possible a slight oxidized surface layer and to avoid a U(VI) release peak. This could mean an overestimation of the uranium released into solution during the leaching tests under anoxic conditions.

1-1-2) Metallic Iron

For one of the leaching tests, iron foil was placed into the system to simulate the carbon steel canister and to stabilize the redox conditions in the leaching experimental device. Rolled 99.99% pure iron foil was supplied by Goodfellow®. The dimensions are 2 cm x 2 cm with a thickness of 125 µm and a weight of 0.64 g. The pure iron foil was rinsed in ethanol and ultrasound-cleaned for 2 minutes before its introduction into the reactor.

1-2) Leaching experiments

Four leaching tests were performed under static conditions (i.e. without renewal of the solution). Environmental constraints are added in stages and are therefore increasingly complex. The simplest system is carbonated water and the most complex involves synthetic Cox groundwater with corroded metallic iron. The experimental conditions are listed in Table 2.

1-2-1) Leaching reactors setup

The leaching experiments were performed inside a glove box under an argon atmosphere (O_2 <1 ppm). This glove box is under a slight depression with respect to the laboratory atmosphere in order to avoid any risk of plutonium contamination. The hermetic reactors are made of titanium and the surfaces covered with a titanium oxide layer which remains chemically inert towards the species in solution. Thanks to a slight overpressure of 3.5 bars in the reactor, samples of solution are taken over time by simply opening a valve without opening the reactor and disturbing its atmosphere.

1-2-2) in carbonated water with and without H_2

Two leaching experiments were carried out in carbonated water. For each experiment, two Mimas® MOX pellets were introduced inside a reactor filled with 155 mL of carbonated water ($NaHCO_3$ 10^{-2} M). The pH was around 9.2±0.3 for both experiments. The first benchmark experiment took place under argon while the second was performed in the presence of hydrogenated argon (Ar/H_2 70/30%). The initial pressures were 3.5 bars for the two experiments while for the one with H_2, the pressure was increased to 5 bars after 322 days of leaching. Table 3 gives the evolution of the pressures measured as a function of time. Samples of the solution were taken over time. To evaluate the presence of colloids in solution the last sample was filtered and ultra-filtered. The filter cut-off thresholds were 0.45 µm (VWR cellulose acetate filter) and 0.02 µm (Whatman Anodisc inorganic filter), respectively.

At the end of the experiment, the corroded pellets were stored under argon to preserve them before characterizations. The leachate was collected and acidified in a separate bottle at a concentration of 0.5 M HNO_3. After 24 hours, a sample of this acidified leachate was taken for liquid analysis. The titanium reactor was also submitted to successive acidic rinses with nitric acid for 24 hours with an acidity reaching 2 M, then for a further 24 hours with an acidity of 0.5 M. Finally three rinses with deionized water were carried out. The full rinse procedure specifically makes it possible to determine the amounts of actinides sorbed and/or precipitated on the walls of the reactor.

1-2-3) in synthetic Cox groundwater

Synthetic Cox water simulating Cox claystone groundwater was used for the leaching tests. Its chemical composition has been validated by Andra (French National Radioactive Waste Management Agency) as being representative of that of the French Underground Research Laboratory (URL) located in Meuse/Haute Marne (France) [23]. The chemical composition is detailed in Table 4 and the pH is around 7.2±0.3. The synthesis protocol of this water is described in detail in Tribet et al. [24].

Two MOX pellets were introduced inside a reactor filled with 155 mL of synthetic Cox groundwater solution. The solution was first purged with Ar/CO_2 3000 ppm for 2 hours, and then an overpressure of 3.5 bars was applied to allow solution sampling over time. To evaluate the presence of colloids in solution, the last sample was filtered and ultra-filtered as for the experiments in carbonated water. The filter cut-off thresholds were again 0.45 µm (VWR cellulose acetate filter) and 0.02 µm (Whatman Anodisc inorganic filter), respectively. The experiment was stopped according to the same protocols as those described for carbonated water.

1-2-4) in synthetic Cox groundwater with metallic iron

Iron pre-corrosion step

An iron foil was placed in the autoclave to simulate container corrosion products and to move towards realistic reducing conditions in the absence of the fuel pellet. Such reducing conditions are expected in deep geological disposal. The iron foil was placed a few centimeters under the sample holder accommodating the MOX fuel pellets. The duration of this pre-corrosion step was 111 days during which the iron foil was corroded in the presence of synthetic Cox groundwater. After closing the reactor the solution was purged with Ar/CO_2 3000 ppm for 2.5 hours, and then an overpressure of 3.5 bars was applied to allow solution sampling. Solution samples were taken over time in order to monitor the evolution of iron concentration in the solution. This step made it possible to form corrosion products on the surface of the iron foil and to add the Fe^{2+} reactive species to the chemistry of the synthetic Cox groundwater.

MOX corrosion step

At the end of the pre-corrosion step, two MOX fuel pellets were introduced into the reactor. The solution was purged with Ar/CO_2 3000 ppm for 30 minutes and the reactor pressurized again to 3.5 bars. The solution samplings and the end of the experiment were carried out as for the previous experiments in carbonated water or synthetic Cox groundwater. At the end of the experiment, the corroded pellets and the iron foil were stored under argon to preserve them before surface characterizations.

Recovery of the sorbed uranium on the iron foil

Once the iron foil characterized, it was immersed in a nitric acid solution at a concentration of 0.5 M in order to release the sorbed uranium. A solution sample was taken for analysis and acidified to 3 M to prevent formation of iron hydroxide in solution once the sample had been taken out of the glove box. The final objective here was to carry out mass balances and to determine the total amount of uranium which could have precipitated on the surface of the iron foil during the leaching experiment.

1-3) Analysis techniques

1-3-1) in solution

The redox potential (Eh) of the solutions was measured using a commercial WTW SenTix® ORP electrode. Measurements were carried out in samples of solution coming from the reactor (ex-situ measurements) or directly inside the reactor at the end of the leaching experiments (in-situ measurements). The pH was also measured with a Mettler Toledo Ingold LoT406-M6-DXK-S7/25 electrode. These two parameters (Eh and pH) are important and strongly affect the speciation of actinides in solution.

Uranium in solution was analyzed by laser-induced kinetic phosphorescence with a Chemchek KPA11 Kinetic Phosphorescence Analyzer (quantification limit 0.1 $\mu g.L^{-1}$). A mineralization step consisting in evaporating the solution followed by dissolution of the residue in an acidic medium was necessary to avoid signal extinction.

Alpha counting (Eurisys IN20 α-β multidetector counter) combined with alpha spectrometry (Canberra α Analyst spectrometer) were used to analyze plutonium in solution. The quantification limit of these radiometric techniques was 0.1 $Bq.mL^{-1}$. The solutions were diluted by a factor of 5 before measurement in order to avoid the formation of a salt by evaporation of the micro-deposit on a stainless steel disc. The precipitation of a salt prevents alpha particles from reaching the detectors because of attenuation in the salt layer. Traces of plutonium were detected after dilution but the activities measured were less than 0.1 $Bq.mL^{-1}$, which did not allow a quantification of the plutonium in the Cox water, the latter being only slightly released in solution. Only the experiments in carbonated water led to measurable and quantifiable α activities in the solutions.

The main cations in solutions (Fe, Ca, Mg, K, Na, Si, and Sr) were analyzed by Inductively Coupled Plasma Atomic Emission Spectroscopy (Jobin Yvon JY46 ICP-AES) and the anions (Cl^- and SO_4^{2-}) by ion chromatography with a METROHM COMPACT 881 PRO chromatograph.

1-3-2) in the gas phase of the reactor

A MicroGC 3000 gas chromatograph from SRA Instruments was used for the gas phase analysis above the leachate. This equipment allows gas phase analysis (H_2, O_2, N_2, and He) with a detection limit of 1 ppm. The gas phase analysis allows to quantify the production of hydrogen during the corrosion step of the iron foil under anoxic conditions. It also makes it possible to check the hydrogen content in the reactor when a hydrogen overpressure is applied. Hydrogen analyzes were carried out mainly at the start or at the end of the experiment to guarantee its content and in order to avoid significant departures during gas flushing and purging of the analysis line.

1-3-3) Characterizations of corroded surfaces

A ZEISS SUPRA 55 WDX microscope was used to characterize the MOX pellets and iron foil surfaces by Scanning Electron Microscopy (SEM). An accelerating voltage of between 5 and 20 kV was applied for imaging, and 20 kV for EDX analyses.

Raman spectroscopy was implemented in order to identify the secondary phases formed. This technique in remote mode makes it possible to characterize radioactive samples without sample preparation. The equipment was a Jobin-Yvon Labram HR800 spectrometer with a laser excitation at 532 nm coupled to an optical microscope. The remote connection between the optical microscope and

the spectrometer was ensured by optical fibers. The conditions of use have been optimized in order to avoid as much as possible heating and oxidation of the surfaces exposed to the laser beam. An optical lens with a magnification of x100 and a low laser power of 0.6 mW were selected [25].

For characterization by X-ray Absorption spectroscopy (XAS), the corrosion products were sampled by slightly pressing, a polyimide adhesive tape (kapton®) onto the MOX corroded surface, then it peeling off. This resulted in the presence of a visibly heterogeneous deposit on the tape surface. The sample was then encapsulated in double containment to prevent contamination.

XAS characterization was performed on the MARS beamline at the synchrotron SOLEIL [26] with a beam size of 0.3×0.3 mm^2. The monochromator energy was calibrated by setting the first inflexion point of the absorption K-edge of metal iron to 7112 eV. The sample holder was positioned vertically and oriented at 35° compared to the incident X-ray beam to prevent polarization effects [27]. The sample surface was scanned to find areas of significant Fe concentrations. Next, spectra were collected at successive positions on areas of significant Fe signal. The beam was moved between scans to avoid sample damage. The scans obtained were compared and found to be similar. They were summed up to obtain a single spectrum with satisfactory signal-to noise ratio. Spectra were also collected in transmission mode on Fe-containing references.

Data were reduced and normalized following standard procedures, using the Athena-Artemis interfaces to Ifeffit [28]. Extended X-ray Absorption Fine Structure (EXAFS) spectra were normalized with respect to the main absorption edge. Fourier transform (FT) of the EXAFS data display amplitude maxima at R + ΔR positions, shifted by ΔR = -0.5 to -0.5 Å with respect to the structural length of the corresponding scattering path. Data were modeled in R space using phase and amplitude functions calculated with FEFF 8.4, and the structure of nontronite [29] and akaganeite [30] as reference environments.

1-4) Geochemical modeling and thermodynamic database

The saturation index and solubility of secondary U phases with respect to synthetic Cox claystone groundwater were calculated with the geochemical module CHESS [31] using the truncated-Davies activity correction model. Simplified activity-activity diagrams of uranium speciation were also calculated with CHESS. The thermodynamic database ThermoChimie [32], version 9, were considered for the calculations. The recent data on the coffinite formation constant at 25°C [33] (1 U^{4+} + 1 H_4SiO_4 - 4 H^+ => $USiO_4$, $logK_f$ = 5.3) was used instead of the ThermoChimie formation constant ($logK_f$ = 7.8).

2) Experimental results

2-1) Uranium concentrations in solution

Figure 1 shows the change in U concentrations over time for the three systems: carbonated water, synthetic Cox groundwater and synthetic Cox groundwater in the presence of a corroded iron foil. Environmental conditions have a significant effect on U concentrations and changes over time. In carbonated water, U concentrations increase with an almost linear trend to reach $8.3x10^{-5}$ mol.L^{-1}, which points to a continuous oxidative dissolution of the $U_{1-x}Pu_xO_2$ matrix under the effect of α radiolysis of water. Moreover, carbonates have a strong complexing ability in solution with respect to uranyl ions that prevents precipitation of secondary U phases on the fuel surface. Uranium is therefore a good tracer of the oxidative dissolution of the MOX pellet.

In synthetic Cox groundwater, a significant (three orders of magnitude) drop in U concentrations can be observed, which indicates a considerable effect of water chemistry on releases. However, the concentrations increase slightly over time, ranging from $4.8x10^{-8}$ mol.L^{-1} after 15 days of leaching to $7.25x10^{-8}$ mol.L^{-1} at the end of the test (222 days). This slight increase reflects a slow but continuous dissolution of the $U_{1-x}Pu_xO_2$ matrix without reaching a steady state. For the carbonated water and synthetic Cox groundwater systems, the presence of colloids was not observed since the unfiltered, filtered, and ultrafiltered concentrations were the same. For the synthetic Cox groundwater + iron system, the concentrations are even lower and drop to $4.0x10^{-10}$ mol.L^{-1} after 96 days of leaching. This steady-state concentration is within the range of data reported in the literature for the solubility of the amorphous U hydroxide $UO_2.xH_2O$(am) [34]. The dashed lines in Figure 1 stands for the solubility calculated with respect to the reaction of formation 1 U^{4+} + 4 H_2O - 4 H^+ => $UO_2.2H_2O$ (am). The upper solubility limit ($4.0x10^{-9}$ mol.L^{-1}) was calculated with the Thermochimie constant $logK_f$ of -1.5. The lower solubility limit ($4.0x10^{-10}$ mol.L^{-1}) of the literature at circum-neutral pH [34] was calculated with a $logK_f$ value of -0.6. Eventually, it is worth noting that this study found a higher U concentration close to $1.3x10^{-8}$ mol.L^{-1}, in the first days of leaching (2 days) indicating the initial presence of U(VI) despite the precautions taken to control the initial oxidation state of the pellets. The high α activity of the pellets and the handling in a glove box (PO_2 <1ppm and possible trace of water) do not allow to avoid a slight surface oxidation and the formation of UO_{2+x}.

Figure 2 shows the evolution of U concentrations for carbonated water and carbonated water + Ar/H_2 systems. It appears that the addition of H_2 does not have a significant effect on the U concentrations measured compared to the benchmark experiment without H_2. After 332 days, the concentrations are the same, around $8.0x10^{-5}$ mol.L^{-1}. However, it should be noted that there is a difference in the initial release profiles since a slowing down is observed in the presence of H_2 during the first days unlike the situation for the carbonated water system. This slowdown is again observed when the Ar/H_2 pressure (70/30%) is increased to 5 bars after 322 days of leaching, but the U concentrations increase continuously over the long term. Hydrogen therefore does not reduce U releases for dissolved

concentrations up to $1.2x10^{-3}$ mol.L^{-1} (i.e. a H_2 partial pressure of 1.5 bars) and for this kind of MOX fuel sample with a high α activity of $1.3x10^{9}$ Bq.g^{-1}.

2-2) Distribution of released U and Pu among aqueous, colloidal and sorbed phases

Figure 3 shows the distribution of the total U released between the soluble, the colloidal and the sorbed parts on the experimental set-up for the three systems: carbonated water, synthetic Cox groundwater and synthetic Cox groundwater in the presence of iron. This distribution is very different for the carbonated water experiment where the soluble part is predominant. For the other two systems, most of the released U is recovered on the walls of the reactors. Nevertheless, in terms of total sorbed quantities there are 36 (±2) µg (i.e. only 1.4% of the total release) in carbonated water and 44 (±3) µg (95.7%, i.e. almost all of the release) in synthetic Cox groundwater. The sorbed quantities are therefore comparable in synthetic Cox groundwater and in carbonated water where the predominance of the uranyl ion is expected. The difference in the percentages is mainly due to the low concentrations measured in the synthetic Cox groundwater. For the synthetic Cox groundwater + iron foil system, the amounts sorbed are low, with around 7.3 (±0.3) µg (i.e. 91.3% of total release) on the walls of the reactor and only 0.4 (±0.1) µg on the iron foil (i.e. 5.0% of the total release). Finally, Figure 3 clearly shows a significant drop in the total quantities of U released when the system becomes more complex. The total quantities are 2500 (±200), 46 (±3), and 8 (±0.5) µg for the carbonated water, synthetic Cox groundwater and synthetic Cox groundwater + iron foil systems, respectively.

Figure 4 shows the distribution of U and Pu released after 559 days of leaching for the carbonated water + Ar/H_2 (30%) experiment. Plutonium is equally distributed between the solution, the colloidal and the sorbed fractions on the walls of the reactor. For U species, the behavior is the same as that observed in the presence of a carbonated water alone, with most of it in the solution. The total amount of U released (4560 (±220) µg) remains much higher than that of Pu (17 (±2) µg) indicating a strong incongruence of releases. In fact, a dissolution of the pellet in the molar ratios of the fuel pellet (U / Pu) would lead to U to Pu release ratios of around 12.4, compared to the approximately 270 experimentally measured.

2-3) Cox groundwater chemistry and redox conditions

None of the Cox groundwater elements (K, Na, Ca, Mg, Sr, Si, Cl^-, SO_4^{2-}) showed important evolution in concentration over the duration of the experiments, i.e. less than 3 % corresponding to the uncertainty on the analysis by ICP-AES. The pH was around 7.3 (±0.2) for the leaching experiment in Cox water and around 7.8 (±0.1) with the iron foil.

The redox potential Eh measured *ex situ* (i.e. in the samplings) was about +260 (±20) mV/SHE for the leaching experiment in Cox water, and rose to +410 (±10) mV/SHE for the *in situ* measurement (i.e. in the leachate) when the reactor was opened. For the experiment with metallic iron, the Eh measurements were not stable and were around +80 (±30) mV/SHE, which is high given the reducing conditions expected. Measurements between -50 and -100 mV/SHE were, however, obtained at the end of the pre-corrosion step and before the MOX pellets were added. This redox potential measurement remains only indicative because the *in situ* measurement at the end of the leaching experiment required the reactor to be opened which also disrupts the composition of the gas phase and promotes the departure of hydrogen in the glove box. Moreover, the *ex situ* measurements are not representative of the leachate in the closed reactor since they are done in a sample bottle.

Eventually, the present set-up for measuring the Eh potential only gave an estimation of the redox potential within the bulk solution and not a local measurement at the very surface of the MOX pellet. However, Eh data were found meaningful from a semi-quantitative and relative point of view while comparing the different experimental conditions and discussing the Pu and U solubilities.

Regarding the levels of reducing species for the Cox groundwater leaching experiment with iron, the Fe concentrations stabilized at 1.6×10^{-4} mol.L^{-1} during the pre-corrosion step (111 days). They did not change during the leaching experiment in the presence of MOX pellets (278 days), with an average content of 1.8×10^{-4} mol.L^{-1}. The samples were clear and no trace of colloids was detected after ultra-filtration, which implies the predominance of Fe(II) species in solution. The H_2 content measured in the reactor atmosphere at the end of the pre-corrosion step at 111 days was 1400 ppm (i.e. 5×10^{-3} bar) and 1225 ppm (i.e. 4.3×10^{-3} bar) after 278 days of leaching. This H_2 mainly comes from the anoxic corrosion of the iron foil and the water radiolysis.

2-4) Characterizations of MOX fuel pellets

2-4-1) Cox synthetic water

For the Cox water experiment, very few precipitates are observed on the pellet surface (Figure 5a-b) and grains of a few microns characteristic of the MOX fuel microstructure are still visible (Figure 5c-d). These precipitates are essentially particles of nano or micrometric size dispersed on the surface of the pellet (Figure 5b-d). Some precipitates form small balls from a few hundred nanometers to a few microns in diameter. EDX analyses of these balls mainly show the presence of Si, Mg, Al, and U. A semi-quantitative analysis of these elements gives atomic percentages around 35, 9, 27 and 23 at.%, respectively. The chemical elements Si, Mg and Al come from the synthetic Cox groundwater and the U from the MOX fuel pellet. The presence of U can potentially result from an interaction between the analysis probe and the fuel substrate or indicate the formation of U-based silicate phases, since larger

balls (a few microns) also indicate its presence. Note that calcium was detected on the surface of the pellets mainly as Ca sulfate precipitates such as gypsum or anhydrite. Precipitates containing Na, K and Cl were also detected, possibly forming during the drying of the samples.

2-4-2) Cox synthetic water with corroded iron foil

During the experiment in the presence of iron, the MOx surface was completely covered by a precipitate (Figure 6 a-b) with granule shapes and rounded concretions of micrometric and submicrometric sizes (Figure 6c-d). No trace of U is detected in this layer, which is several microns thick. EDX analyses of the granules mainly show the presence of Fe and Si. A semi-quantitative analysis of these elements leads to atomic percentages of around 85 and 10 at.%, respectively. Some traces of Cl, Al, and Ca are also detected, but at low levels of 1 to 2 at.%. Therefore, it is mainly a Fe-containing precipitate that formed at the fuel/water interface by oxidation of Fe(II) to Fe(III). Previous work has concluded that iron hydroxide such as akaganeite (β-FeOOH) precipitates on the surface of UO_2 pellets subjected to α irradiation [25] in the presence of Cox water containing chlorides. Figure 7 shows the Raman spectrum of the layer observed at the MOX pellet surface in the presence of iron. Fairly wide Raman bands can be seen between 310 and 390 cm^{-1} and a wide band around 700-720 cm^{-1}. This Raman spectrum is compatible with the formation of an Fe oxyhydroxide quite similar to akaganeite. However, a band at 344 cm^{-1} is observed between the two bands at 311 and 390 cm^{-1} of akaganeite. This band at 344 cm^{-1} is also close to the data of de Faria [35] on maghemite characterized by bands at 700 cm^{-1} and 350 cm^{-1}. This slight difference compared to previous work [25] may be due to a partial phase modification under the effect of the laser beam. Despite the precautions taken, the laser power may have been slightly too high and induced a transformation of the oxy-hydroxide into maghemite and a mixture of phases [36].

Additional characterization of the Fe-containing corrosion products was performed by XAS. In addition to carbonate and oxyhydroxide corrosion products, the literature on the corrosion of carbon-steel in a clay environment [37-39], either as synthetic clayey water or solid interface with clay rocks or bentonites), have demonstrated the occurrence of several secondary Fe(II/III)-silicates (berthierine $(Fe_2Al)(SiAl)O_5(OH)_4$, chamosite $Fe_5Al(AlSi_3)O_{10}(OH)_8$, cronstedtite $Fe_3SiAlO_5(OH)_4$, greenalite $Fe_3Si_2O_5(OH)_4$), and Fe(III)-silicates (nontronite $Ca_{0.17}Fe_{1.67}Al_{0.67}Si_{3.66}O_{10}(OH)_2$). All the spectra of such possible corrosion products (Figure 8) show a small pre-edge feature at 7114 eV, predominantly corresponding to a 1s→3d (quadrupole). This transition is electric-dipole forbidden in centrosymmetric (e.g. octahedral) environments but its intensity can be substantially increased in tetrahedral environments by the mixing of Fe 3d and ligands p orbitals. Here the weak amplitude suggests that Fe is predominantly six-fold coordinated by O [40, 41]. The energy position of this feature

compares to Fe(III)-containing references such as goethite (α-FeOOH), lepidocrocite (γ-FeOOH), hematite (α-Fe_2O_3), or maghemite (γ-Fe_2O_3). In comparison, the pre-edge peak is located at a significantly lower energy of 7112 eV for the Fe(II)-bearing minerals siderite ($FeCO_3$) or greenalite ($Fe_3Si_2O_5(OH)_4$). This observation indicates that the Fe is mostly at an oxidation state of +III.

This oxidation state of Fe is further supported by comparison of the XANES spectra for the Fe-MOX with references. Figure 8 (see also Figure (a) in supplementary material section) shows that the edges positions cluster as a function of the oxidation state of Fe. The half-edge energy is lowest for Fe(II)-containing siderite (7119.4 eV), slightly higher for greenalite and chamosite (7120.4 eV), even higher for berthierine and cronstedtite (7121.7 and 7122.2 eV, respectively), and reaches 7123.7-7125.0 eV for Fe(III) compounds. The edge for the Fe-MOX (7123.3 eV) clearly plots with the Fe(III) references, and is significantly shifted compared to the Fe(II) containing reference. This confirms that Fe(II), if present in the sample, is marginal at best.

The EXAFS spectrum for Fe-MOX displays several oscillations with distinct frequencies (Figure 9a), indicating that Fe is surrounded by several backscattering shells. This inference is confirmed by the presence of several peaks on the FT (Figure 9b). The first peak near R + ΔR = 1.5 Å corresponds to the contribution of O shells. The best fit (Table 5) was obtained by assuming a split coordination sphere of O atoms with coordination numbers $N_{O_1} = 3.1$ and N_{O_2}= 3.0 at distances of R_{O_1},= 1.92 Å and R_{O_2},= 2.06 Å, respectively. The average Fe-O distance (1.99 Å) is consistent with the average distance observed for Fe(III) in a distorted octahedral site, as in goethite or akaganeite. The FT also displays one peak at 2.7 Å and a shoulder near 3.2 Å, suggesting the presence of at least two additional shells. Due to the amplitude of these peaks and the similarity of the EXAFS spectrum with Fe oxyhydroxides, it was surmised that these two shells were made of Fe contributions. A correct fit was obtained by assuming the presence of two Fe shells at ~3 and 3.5 Å, but the shoulder was improperly accounted for. This suggested the presence of a third additional contribution at a greater distance, possibly corresponding to Fe, O, or multiple scattering. Multiple scattering was ruled out due to the disported nature of the O coordination sphere, a decision corroborated by FEFF calculations showing that the amplitude of these contributions was only a fraction of single scattering paths. To better identify the nature of this contribution, the Fourier-filtered data and fits were compared in the reciprocal space (q, in $Å^{-1}$). This comparison revealed that most of the misfit originated from a q-range around 4 $Å^{-1}$, suggesting that it is due to the contribution of rather light atoms, for which the amplitude is maximal. Eventually, a correct fit was obtained by including O atoms at 4.2 Å from central Fe. Note that the presence of such shells can be anticipated from the crystallographic structure of Fe(III) hydroxide. Finally, the best fit was obtained assuming 1.6(5) and 1.8(7) Fe atoms at 3.01 and 3.46 Å, respectively. The distance values compare favorably with the structure of akaganeite, in which Fe is surrounded by 2 Fe neighbors at

3.03 Å, and three pairs of Fe neighbors at 3.34, 3.51, and 3.56 Å, respectively. This corresponds well to the environment expected for Fe(III) oxyhydroxide, in which a Fe(III) octahedral shares edge and corners with adjacent octahedra, resulting in Fe-Fe distances of 3.03 and 3.30-3.5 Å, respectively. The reduced number of neighboring Fe suggests that such clusters are reduced in size, consistent with the poor resolution of Raman spectra.

In conclusion, XAS analysis indicates that the Fe in the corrosion product is in an oxidation state of +III, and is six-fold coordinated by O. It is present in small oxyhydroxide domains, by sharing edges and corners with adjacent octahedra. This environment is compatible with the formation of small-size akaganeite-like domains.

2-4-3) Carbonated water with hydrogen

Unlike the Cox water experiments with and without iron, the carbonated water experiment with H_2 leads to a pronounced corrosion of the surface as shown in Figure 10. The alteration is strongly heterogeneous throughout the pellet. The experiment in carbonated water and without H_2 leads to the same observations. Significant corrosion pits and U losses can be observed and have characteristic sizes corresponding to the initial grains of the ceramic (5 to 10 µm). These areas analysed by EDX (Spectrum 2 - Figure 10c) are characterized by low Pu contents (1 to 2 at.%). In contrast, the zones with the highest Pu contents (from 10 to 28 at.%) are clearly less corroded or even almost intact (Spectrum 1,3 and 4 - Figure 10b-c). These observations confirm that under these experimental conditions, H_2 does not inhibit the oxidative dissolution of the MOX fuel. Moreover, the U released into the solution mainly comes from areas with a low Pu content.

2-5) Characterizations of corroded iron foil

The surface of the iron foil was also observed by SEM at the end of the leaching experiment (see Figure (b) and (c) in supplementary material section). Very few precipitates are detected on the surface which seems slightly corroded. Two types of precipitates can however be distinguished:

- A phase with a morphology based on balls of needles and plates. The average elemental composition analyzed by EDX (8 points) is approximately 84 at.% Fe, 12 at.% Na, 3 at.% Cl, K. Unfortunately, this phase was not detectable with the optical microscope coupled to the Raman spectrometer and therefore could not be characterized by that technique. A corrosion product such as Fe hydroxide or Fe hydroxy-carbonate seems the most likely, since the O, H and C elements are not detectable by EDX. Furthermore, the morphology observed is close to that of the chukanovite ($Fe_2(CO_3)(OH)_2$) phase detected and characterized by Raman spectroscopy in a previous work with similar corrosion conditions [25].

- Precipitates composed of nano to micrometric particles were also detected on the iron foil. Their EDX analyses showed the presence of U in significant amounts (70.25 at.%). The Fe signal (29.75 at.%) can come from the iron foil given the size of the precipitate with respect to the EDX analysis depth, which is around 1 µm. This chemical composition which indicates the strong presence of U (possibly with O, H or C which cannot be detected by EDX) and the very low concentrations of U measured into the solution are fully compatible with the presence of an amorphous U hydroxide $UO_2 \bullet xH_2O$ (am).

3) Discussion

3-1) Influence of environmental water chemistry on alteration

The influence of chemical species dissolved in groundwater on the oxidative dissolution of UO_2 has been the subject of numerous studies [42-46]. These studies have shown a significant effect of Si and divalent cations (Ca^{2+} or Mg^{2+}) on UO_2 dissolution assigned to two different mechanisms:

- the precipitation of a secondary phase which could act as a diffusion barrier (physical barrier) against oxidizing species, water and ions [42, 45, 46] or simply reduces the concentrations of U in solution by consuming it by precipitation,
- or an oxidation inhibition mechanism that would prevent U oxidation at the surface up to the +VI oxidation state [43, 44].

In all cases, the authors observe a noticeable effect of the groundwater chemistry; whether the studies involved studies carried out electrochemically [44] or were based on measurements of U release into the solution [45]. With regard to the MOX fuel pellets leached in this study, Si and divalent cations (Mg^{2+} and Ca^{2+}) were well detected on the surface, which argues for a similar effect to that observed on UO_2-based fuels. In addition, the preferential dissolution of UO_2 grains observed for the Mimas® MOX fuel in carbonated water should also be limited by the groundwater chemistry, as is the case for UO_2-based fuels.

Concerning the precipitation of a secondary phase, the conservative assumption of an uninhibited oxidative dissolution of the MOX fuel followed by a complete U reprecipitation at the surface of the pellets should have led to precipitate thicknesses between 1.5 and 3 µm. This simple calculation takes into account the total amount of U released in carbonated water ($8.6x10^{-6}$ mol_U) assuming that the oxidative dissolution is fully effective, the surface area of the pellets and the densities of expected U silicates, i.e. 4.6 $g.cm^{-3}$ for soddyite [$(UO_2)_2SiO_4{:}2H_2O$] and 3.9 $g.cm^{-3}$ for uranophane [$Ca(UO_2)_2(SiO_3OH)_2{:}5H_2O$)] [47]. However, no oxidized U secondary phase was detected on the surface of the pellets at the μm^3 scale. This point is consistent with the negative saturation indexes (under

saturation state) calculated on the basis of the water chemistry and reported in Table 6. Note that taking into account the ternary complexes $Ca_2UO_2(CO_3)_3$ and $CaUO_2(CO_3)_3^{2-}$ [48] strongly modifies the U speciation in solution and decreases the value of the calculated saturation indexes. However, the saturation indexes remain negative even if these complexes are not taken into account, which indicates that the experimental conditions are not conducive to the precipitation of the U secondary phases tested. In terms of U concentrations, the experimental data which are around $5x10^{-8}$ mol.L^{-1} remain much lower than the concentrations calculated with CHESS for the complete chemistry of the synthetic Cox groundwater. The calculated concentrations are $6x10^{-4}$ and $3x10^{-4}$ mol.L^{-1} for soddyite (synt2) with and without ternary complexes, respectively. The concentrations are $6x10^{-5}$ and $9x10^{-7}$ mol.L^{-1} for uranophane with and without the ternary complexes, respectively. Uranophane would, therefore, be the least soluble phase. Uranophane solubility limits are also plotted in the Eh-activity diagram of Figure 11 for a simplified Cox chemistry. Furthermore, the possibility of coffinite precipitation, which is an unoxidized U(IV) silicate with the formula $USiO_4$, was also evaluated on the basis of recent thermodynamic data [33]. Figure 11 shows that the stability domain of coffinite coincides with reducing potentials. This point could be disputed on the basis of recent work which has shown that coffinite can also be formed under slightly oxidizing conditions of, up to +100 mV and in the presence of UO_{2+x} [49]. Regarding the oxidizing conditions of the synthetic Cox groundwater (+410 (±10) mV/SHE for the *in situ* measurement) and the absence of reducing species in the solution, coffinite is not liable to precipitate under such conditions.

The second possible mechanism is based on an inhibition of oxidative dissolution due to the presence of divalent cations and Si at the surface. These elements would not disturb the oxidation of $U^{IV}O_2$ to $U^{IV}_{1-2x}U^{V}_{2x}O_{2+x}$, but would then suppress the conversion of $U^{IV}_{1-2x}U^{V}_{2x}O_{2+x}$ into $UO_3.yH_2O$ [43, 44, 50] by adsorbing at the surface and by modifying anionic transfers. More recently, an inhibiting effect has been allocated to calcium, considering that the formation of a low solubility Ca-U(VI) compound reduces oxidative dissolution [42] and could play a passivating role. We cannot exclude the presence of such a phase or a silicate in our study on very low thicknesses, since these elements were detected on the surface.

In the end, a mechanism of dissolution inhibition due to the presence of Si and divalents (Ca^{2+}or Mg^{2+}) elements on the surface may be the most plausible explanation for the drop in U concentrations in synthetic Cox groundwater, rather than a simple dissolution/precipitation process without any lowering of the oxidative dissolution.

3-2) The role of the active redox species iron and hydrogen

The effects of iron and hydrogen produced by the anoxic corrosion of containers on the behavior of actinides and redox-sensitive radionuclides have also been the subject of numerous studies. In general, reducing conditions have a significant effect on the oxidative dissolution of UO_2 and $(U,Pu)O_2$ based fuels [8, 9, 11, 25].

3-2-1) Role of H_2

An inhibiting effect of H_2 has been observed both on UOX and MOX spent fuel irradiated inside nuclear reactors [8, 13, 14, 18], on nuclear fuel surrogates [51] and on actinide oxides which are mainly α emitters [20, 52, 53]. The activation of molecular H_2 (reaction R1), which is effective at low temperature, hinders U oxidation (R2) and neutralizes oxidizing species at the fuel/water interface [52]. This activation results from the catalytic properties of the ε metallic particles for spent fuel [54] but also from the catalytic properties of actinide oxide surfaces subjected to a single α irradiation field [20, 52].

$$\mathrm{H_2} \xrightarrow{\text{epsilon particle and U(IV)–U(V) site}} 2\mathrm{H^{\circ}} \qquad (R1)$$

$$\mathrm{U(V)} + \mathrm{H^{\circ}} \rightarrow \mathrm{U(IV)} + \mathrm{H^{+}} \qquad (R2)$$

In fact, the unique electronic structure of light actinides with an overlap of the 5f, 6d and 7s bands makes them good potential catalysts like transition metals [55]. As shown in Figure 2, no significant long-term effect of H_2 was observed on the oxidative dissolution of the Mimas® MOX fuel for a H_2 concentration going up to 1.2×10^{-3} mol.L^{-1} (i.e. 1.5 bars of H_2 gas) and an α activity of 1.3×10^{9} Bq.g^{-1}. However recent work on a Mimas® MOX fuel [20] with a high Pu content (24 wt.%) and a higher α activity (4.96×10^{9} Bq.g^{-1}) showed that an inhibiting effect can be observed as for simple α -doped UO_2 [53]. It should be noted that low stabilized U concentrations are maintained during the first month of leaching for this study [20], and then they increase for H_2 concentrations below 6.4×10^{-3} mol.L^{-1}. Figure 2 shows that the H_2 content is therefore not high enough for the Mimas® MOX fuel with an α activity of 1.3×10^{9} Bq.g^{-1}. Nevertheless, H_2 has a slight effect over the first few days of leaching, as shown in the box in Figure 2. These two studies are finally not opposed. They show that the limit H_2 content depends on the α activity of the fuel, and that in the future it will be necessary to specify the conditions (i.e. α activity and H_2 content) for maintaining this inhibiting effect.

On the other hand, the preferential corrosion of grains with a low Pu content (Figure 10a-b-c) in the presence of H_2 raises a question linked to the microstructure of Mimas® MOX fuel. In fact, the local Pu contents in the UO_2 grains showing a preferential corrosion are approximately 3.5 times lower than the average Pu content of the Mimas® MOX pellet. This means that the local α activity that, leads to

the production of oxidizing species at the extreme surface, is, therefore, around 375 MBq.g^{-1} for the UO_2 grains. For this α activity and for the H_2 content of 1.2x10^{-3} mol.L^{-1} (i.e. 1.5 bars of H_2 gas), an inhibition of the oxidative dissolution should have been observed [53]. One explanation could come from the diffusion in solution of the oxidizing species produced on the surface of the high Pu content areas that adjoin the low-content areas. This diffusion would lead to a local increase in the oxidant concentrations, in particular in the corrosion pits. The average free path of radicals and H_2O_2 in solution ranges from a few microns to a few tens of microns [56], which is fully compatible with the UO_2 grain sizes and those of the Pu-enriched areas.

3-2-2) Role of iron

The role of iron appears to be considerably significant in the oxidative dissolution of the MOX fuel (Figure 1 and Figure 6). It is clear that for the experimental conditions studied, the H_2 mainly produced by the anoxic corrosion of iron, has no significant effect (1400 ppm, 3.8x10^{-6} mol.L^{-1}) since the contents analyzed are much lower than 1.2x10^{-3} mol.L^{-1} (i.e. 1.5 bars of H_2 gas). The behavior of iron is to be compared with the α irradiation conditions on the MOX fuel surface. The immediate availability of Fe(II) in solution at the reaction interface after the pre-corrosion step is an essential point explaining the observations. At the fuel/water interface, which is the location of a significant α radiolysis over a thickness of around forty microns, the consumption of oxidizing species by oxidation of Fe(II) to Fe(III) occurs according to the reactions R3 and R4 [57]:

$$\mathrm{Fe^{2+} + H_2O_2 \rightarrow Fe^{3+} + OH^{\circ} + OH^{-}} \quad (R3)$$

$$\mathrm{Fe^{2+} + OH^{\circ} \rightarrow Fe^{3+} + OH^{-}} \quad (R4)$$

The low solubility of Fe(III) for 7 < pH < 8 then induces massive precipitation of Fe(III) hydroxide (R5) at the reaction interface (Figure 6), as already observed and modeled on α -doped UO_2 pellets [25].

$$\mathrm{Fe^{3+} + 2\ OH^{-} \rightarrow FeOOH + H^{+}} \quad (R5)$$

The redox front spatially delimits the distribution of the oxidizing and reducing areas as described by Ewing [1]. The redox front is located at the fuel/water reaction interface for the α irradiation conditions studied here, which prevents oxidative dissolution. The oxidizing species diffuse from the fuel pellet to the solution, and the reducing species from the iron foil. That is to say, the interface between these two zones is localized at the extreme surface of the fuel for these irradiation conditions. The fact that no trace of Fe(III)-hydroxide precipitation was detected in solution is an indirect proof that the oxidants produced by the radiolysis were locally neutralized and did not diffuse into the solution. The solution

remained clear and the iron concentrations before and after ultrafiltration remained constant around $1.6x10^{-4}$ mol.L^{-1}. Furthermore, the measurement of the redox potential in solution, even if it remains indicative, did not show a significant increase. An intense γ irradiation field could also shift the redox front towards the homogeneous solution, since the production of oxidizing species is not limited to the first microns at the interface due to the centimeter path of γ rays. This evolution and displacement of the redox front has already been observed on MOX spent fuel characterized by a strong β/γ irradiation field [58]. Under these γ irradiation conditions, oxidative dissolution is not inhibited because the dissolved Fe(II) reacts before reaching the fuel pellet. Most of the Fe then precipitates in solution in the form of Fe(III)-hydroxide colloids. The MOX fuel investigated here is mainly α emitter. The calculated residual β/γ dose rates (β contributors: ^{234m}Pa, ^{231}Th, ^{234}Th and γ contributor: ^{241}Am) are clearly negligible in the homogeneous solution, i.e. less than 1 to 2 mGy.h^{-1} (Table 7). The energy deposit is well localized at the reaction interface, as is the production of oxidizing species by water radiolysis. The dose rate of 5640 Gy.h^{-1} is mainly due to α decays [19] because of the presence of Pu.

Regarding the behavior of U, the presence of iron clearly inhibits the oxidative dissolution and leads to a thermodynamic control of the alteration. The consumption of oxidizing species by iron prevents the oxidative dissolution of uranium which dissolves without changing its oxidation state. Condensation of the aqueous species $U(OH)_{4aq}$ leads to the formation of an amorphous hydroxide with a very low solubility and leads to a thermodynamic equilibrium. The U concentrations measured are fully compatible with such a thermodynamic equilibrium involving the amorphous phase $UO_2 \bullet xH_2O(am)$ [34]. The absence of U detected in the iron precipitate at the MOX fuel surface and the small amount of U recovered on the iron foil (only 0.4 µg) also rule out the possibility of high oxidative dissolution followed by a reductive precipitation. The few traces of U observed by SEM (Figure (b) in supplementary material section) and recovered on the iron foil (Figure 3) may originate from i) an initial release of a slight oxidized layer on the surface of the pellets (Figure 1) followed by a reduction/precipitation of U(VI) on the iron foil [59] or ii) from the sorption of U(IV)-based precipitates and colloids [60]. Most of the U found on the walls of the leaching vessel (Figure 3), but again in small quantities (7.34 µg), is compatible with a U(IV) sorption mechanism on the TiO_2 surface. The sorption capacity of U(IV) onto TiO_2 is about 1 atom U.nm^{-2} TiO_2 [61]. The amount of U(IV) possibly sorbed would be 5.7 µg by taking into account this sorption capacity and the surface of the TiO_2 reactor in the present experiment (~150 cm^2). This value is close to the amount of U actually found on TiO_2 (i.e. 7.34 µg). Therefore, the direct U(IV)-sorption onto TiO_2 could be the mechanism explaining the presence of U on the reactor walls. This quantity is also close to that found by Odorowski et al. (2017) with a similar experimental approach performed with α -doped UO_2 pellets (i.e. 7.6 µg), which argues well for a contribution from the experimental device.

3-2-2) The synergistic effects of hydrogen and iron

Synergistic effects of H_2 and Fe^{2+} could be expected at the interface. The dissolved H_2 can react with the OH° radicals created by Fe^{2+} in the Fenton-like reaction (R4) as follows:

$$H_2 + OH^\circ \rightarrow H^\circ + H_2O \quad (R6)$$

The reaction (R6) converts an oxidizing radical OH° ($E°_{(SHE)}$ = 1.8 V) into a reducing one H° ($E°_{(SHE)}$ = -2.3 V). Therefore the combined effect of H_2 and Fe^{2+} could also explain the low U concentrations measured. Nevertheless, the H_2 concentrations (1400 ppm, $3.8x10^{-6}$ mol.L^{-1}) are much lower than those of Fe^{2+} ($1.8x10^{-4}$ mol.L^{-1}) for the conditions of this study and Fe(II) remains highly predominant. Furthermore, the kinetic constant of reaction (R4) is $3.4x10^{8}$ $mol^{-1}.L.s^{-1}$ compared to $3.9x10^{7}$ $mol^{-1}.L.s^{-1}$ for reaction (R6) [62]. Therefore a limited synergistic effect is expected for this study.

3-3) The behavior of Mimas® MOX fuel compared to UO_2 based fuels and consequences for geological disposal

For both MOX and UOX fuels, an oxidative dissolution under α radiolysis has been clearly observed in carbonated water [19, 53]. This dissolution was observed for UO_2 and MOX-based fuels with α activities of 385 MBq.g^{-1} and 1300 MBq.g^{-1}, respectively. Uranium releases are five times greater for MOX fuel compared to UO_2-based fuel, which is consistent with its higher α activity [19, 53]. The oxidative dissolution of MOX unlike that of UO_2, shows a highly heterogeneous character due to variations in local Pu contents. The fluorite structure is even more resistant to oxidative dissolution as the Pu content is high. Recent work on a homogeneous MOX fuel (24 wt.%) attributed this effect to a Pu enrichment of the fuel surface and to a strong catalytic decomposition of H_2O_2 on the MOX fuel surface [63].

In this study, taking the environmental conditions into account (Cox groundwater with or without iron) leads to quite similar behavior between the two kinds of fuels. Synthetic Cox groundwater lowers U concentrations by three orders of magnitude regardless of the fuel [25] and the presence of iron inhibits the oxidative dissolution independently of the α activity of the pellet and of its microstructure. Figure 12 summarizes the alteration mechanisms of Mimas® MOX fuel in the presence of metallic iron. Fe(III) hydroxide precipitates extensively on the MOX fuel surface by consuming oxidizing species and radiolytic products. The precipitated layer is several microns thick and can ultimately limit the production of oxidizing species by stopping α particles. This mechanistic scheme is close to that already proposed on UO_2-based fuels for the same alteration conditions [25]. It is worth mentioning that the inhibiting effect of H_2 has also been observed on Mimas® MOX fuels with high α activities [20] but it does not appear to operate under the experimental conditions tested here.

All of these results confirm a strong analogy in terms of mechanistic behavior between MOX and UO_2-based fuels. Environmental conditions are able to inhibit oxidative dissolution, even for high α activities. A thermodynamic control of the alteration is expected for both MOX fuels and UO_2-based fuels, corresponding to very low U and Pu concentrations in the groundwater. Moreover, under geological disposal conditions, the α activity, which will predominate in the long term, will continuously decrease due to α decay. This decrease is even more favorable to an early inhibition of oxidative dissolution under real environmental conditions.

Conclusions

The oxidative dissolution of an un-irradiated Mimas® MOX fuel under α radiolysis of water has been studied under environmental conditions of increasing complexity.

The results show a significant effect of the clayey groundwater chemistry (a synthetic Cox claystone water) and Fe(II) species on the oxidative dissolution. Uranium concentrations drop by three orders of magnitude in the Cox groundwater compared to carbonated water from 8.3×10^{-5} to 7.25×10^{-8} $mol.L^{-1}$. The presence of Fe(II) in the solution further lowers U concentrations to 4.0×10^{-10} $mol.L^{-1}$ in agreement with a thermodynamic equilibrium with $UO_2 \bullet xH_2O(am)$.

In the synthetic Cox groundwater, the presence of Si and divalent cations (Mg^{2+}, Ca^{2+}) was detected on the surface of the MOX pellets and could have inhibited the dissolution. In presence of corroded metallic iron, Fe(II) inhibits the oxidative dissolution by consuming the radiolytic oxidizing species at the MOX/water interface. This leads to a massive precipitation of iron Fe(III) oxyhydroxide at the MOX fuel surface which was characterized by Raman and X-ray absorption spectroscopies. No noticeable effect of dissolved H_2 on the oxidative dissolution was detected up to H_2 concentrations of 1.2×10^{-3} $mol.L^{-1}$ (i.e. 1.5 bars of H_2 gas). The H_2 content was not sufficient to inhibit oxidative dissolution unlike iron under these experimental conditions.

Finally, the environmental effects observed with groundwater and reducing Fe(II)-species are very similar to those already observed on UO_2-based fuels which supports an analogy of behavior under geological disposal conditions. This point should be qualified given the chemical and microstructural heterogeneities of this Mimas® MOX fuel. These induce a heterogeneous alteration in carbonated water with corrosion pits depending on the local Pu content. The zones with the lowest Pu contents are the most sensitive to oxidative dissolution under water radiolysis while the local α activities are lower. Additional future studies are needed to better understand the role of molecular H_2 by integrating the heterogeneity of the microstructure and chemistry of Mimas® MOX fuel.

Acknowledgements

This study was carried out under the COSTO research program funded jointly by the CEA, ANDRA, and EDF. The authors thank C. Martin (ANDRA), V Blin (CEA), and F. Tocino (EDF) for their in-depth reviews of this article and their advice. The authors are also grateful to their DHA lab colleagues and to the personnel of the Atalante facility and of the MARS beamline at the synchrotron SOLEIL for their technical support.

Author contributions

Christophe Jégou supervised the whole study and wrote the paper. Mélina Odorowski, Valentin Kerleguer, Veronique Broudic carried out the leaching experiments and participated in their definition. Michel Schlegel led the characterization of corrosion products by X-ray absorption spectroscopy and contributed to write the article. Caroline Marques and Gauthier Jouan were responsible for analyses of solutions and solids, respectively. Laurent De Windt supervised the whole study, carried out the geochemical calculations and contributed to write the article. All the authors helped on paper editing.

The raw/processed data required to reproduce these findings cannot be shared at this time due to technical or time limitations.

References

[1] R.C. Ewing, Long-term storage of spent nuclear fuel, Nat. Mater., 14 (2015) 252-257.
[2] D.W. Shoesmith, Fuel corrosion processes under waste disposal conditions, Journal of Nuclear Materials, 282 (2000) 1-31.
[3] T. Fanganel, V.V. Rondinella, J.P. Glatz, T. Wiss, D.H. Wegen, T. Gouder, P. Carbol, D. Serrano-Purroy, D. Papaioannou, Reducing Uncertainties Affecting the Assessment of the Long-Term Corrosion Behavior of Spent Nuclear Fuel, Inorganic Chemistry, 52 (2013) 3491-3509.
[4] L. Wu, Y. Beauregard, Z. Qin, S. Rohani, D.W. Shoesmith, A model for the influence of steel corrosion products on nuclear fuel corrosion under permanent disposal conditions, Corrosion Science, 61 (2012) 83-91.
[5] S. Sunder, D.W. Shoesmith, N.H. Miller, PREDICTION OF THE OXIDATIVE DISSOLUTION RATES OF USED NUCLEAR FUEL IN A GEOLOGICAL DISPOSAL VAULT DUE TO THE ALPHA-RADIOLYSIS OF WATER, in: T. Murakami, R.C. Ewing (Eds.) Scientific Basis for Nuclear Waste Management Xviii, Pts 1 and 2, 1995, pp. 617-624.
[6] T.E. Eriksen, D.W. Shoesmith, M. Jonsson, Radiation induced dissolution of UO2 based nuclear fuel - A critical review of predictive modelling approaches, Journal of Nuclear Materials, 420 (2012) 409-423.
[7] L.D. Wu, Z. Qin, D.W. Shoesmith, An improved model for the corrosion of used nuclear fuel inside a failed waste container under permanent disposal conditions, Corrosion Science, 84 (2014) 85-95.
[8] K. Spahiu, D.Q. Cui, M. Lundstrom, The fate of radiolytic oxidants during spent fuel leaching in the presence of dissolved near field hydrogen, Radiochimica Acta, 92 (2004) 625-629.
[9] D.Q. Cui, J. Low, K. Spahiu, Environmental behaviors of spent nuclear fuel and canister materials, Energy & Environmental Science, 4 (2011) 2537-2545.
[10] D. Cui, J. Low, V.V. Rondinella, K. Spahiu, Hydrogen catalytic effects of nanostructured alloy particles in spent fuel on radionuclide immobilization, Applied Catalysis B-Environmental, 94 (2010) 173-178.
[11] N.Z. Liu, L.D. Wu, Z. Qin, D.W. Shoesmith, Roles of Radiolytic and Externally Generated H-2 in the Corrosion of Fractured Spent Nuclear Fuel, Environmental Science & Technology, 50 (2016) 12348-12355.
[12] M.E. Broczkowski, P.G. Keech, J.J. Noel, D.W. Shoesmith, Corrosion of Uranium Dioxide Containing Simulated Fission Products in Dilute Hydrogen Peroxide and Dissolved Hydrogen, Journal of the Electrochemical Society, 157 (2010) C275-C281.
[13] M.E. Broczkowski, D. Zagidulin, D.W. Shoesmith, The Role of Dissolved Hydrogen on the Corrosion/Dissolution of Spent Nuclear Fuel, in: C.M. Wai, B.J. Mincher (Eds.) Nuclear Energy and the Environment, 2010, pp. 349-380.
[14] P. Fors, P. Carbol, S. Van Winckel, K. Spahiu, Corrosion of high burn-up structured UO2 fuel in presence of dissolved H-2, Journal of Nuclear Materials, 394 (2009) 1-8.
[15] J. Bruno, K. Spahiu, The long-term effect of hydrogen on the UO2 spent fuel stability under anoxic conditions: Findings from the Cigar Lake Natural Analogue study, Applied Geochemistry, 49 (2014) 178-183.
[16] Y. Albinsson, A. Odegaard-Jensen, V.M. Oversby, L.O. Werme, Leaching of spent fuel under anaerobic and reducing conditions, in: R.J. Finch, D.B. Bullen (Eds.) Scientific Basis for Nuclear Waste Management Xxvi, 2003, pp. 407-413.

[17] G. Oudinet, I. Munoz-Viallard, L. Aufore, M.J. Gotta, J.M. Becker, G. Chlarelli, R. Castelli, Characterization of plutonium distribution in MIMAS MOX by image analysis, Journal of Nuclear Materials, 375 (2008) 86-94.
[18] P. Carbol, P. Fors, S. Van Winckel, K. Spahiu, Corrosion of irradiated MOX fuel in presence of dissolved H-2, Journal of Nuclear Materials, 392 (2009) 45-54.
[19] M. Odorowski, C. Jegou, L. De Windt, V. Broudic, S. Peuget, M. Magnin, M. Tribet, C. Martin, Oxidative dissolution of unirradiated Mimas MOX fuel (U/Pu oxides) in carbonated water under oxic and anoxic conditions, Journal of Nuclear Materials, 468 (2016) 17-25.
[20] L. Bauhn, N. Hansson, C. Ekberg, P. Fors, R. Delville, K. Spahiu, The interaction of molecular hydrogen with alpha-radiolytic oxidants on a (U,Pu)O-2 surface, Journal of Nuclear Materials, 505 (2018) 54-61.
[21] M. Amme, R. Pehrman, R. Deutsch, O. Roth, M. Jonsson, Combined effects of Fe(II) and oxidizing radiolysis products on UO2 and PuO2 dissolution in a system containing solid UO2 and PuO2, Journal of Nuclear Materials, 430 (2012) 1-5.
[22] Z. Talip, S. Peuget, M. Magnin, M. Tribet, C. Valot, R. Vauchy, C. Jegou, Characterization of un-irradiated MIMAS MOX fuel by Raman spectroscopy and EPMA, Journal of Nuclear Materials, 499 (2018) 88-97.
[23] E.C. Gaucher, P. Blanc, F. Bardot, G. Braibant, S. Buschaert, C. Crouzet, A. Gautier, J.P. Girard, E. Jacquot, A. Lassin, G. Negrel, C. Tournassat, A. Vinsot, S. Altmann, Modelling the porewater chemistry of the Callovian-Oxfordian formation at a regional scale, Comptes Rendus Geoscience, 338 (2006) 917-930.
[24] M. Tribet, C. Jegou, V. Broudic, C. Marques, P. Rigaux, A. Gavazzi, Leaching of UO2 pellets doped with alpha- emitters (Pu-238/239) in synthetic deep Callovian-Oxfordian groundwater, in: L. Rao, J.G. Tobin, D.K. Shuh (Eds.) Actinides 2009, 2010.
[25] M. Odorowski, C. Jegou, L. De Windt, V. Broudic, G. Jouan, S. Peuget, C. Martin, Effect of metallic iron on the oxidative dissolution of UO2 doped with a radioactive alpha emitter in synthetic Callovian-Oxfordian groundwater, Geochimica Et Cosmochimica Acta, 219 (2017) 1-21.
[26] I. Llorens, P.L. Solari, B. Sitaud, R. Bes, S. Cammelli, H. Hermange, G. Othmane, S. Safi, P. Moisy, S. Wahu, C. Bresson, M.L. Schlegel, D. Menut, J.L. Bechade, P. Martin, J.L. Hazemann, O. Proux, C. Den Auwer, X-ray absorption spectroscopy investigations on radioactive matter using MARS beamline at SOLEIL synchrotron, Radiochimica Acta, 102 (2014) 957-972.
[27] A. Manceau, D. Bonnin, W.E.E. Stone, J. Sanz, DISTRIBUTION OF FE IN THE OCTAHEDRAL SHEET OF TRIOCTAHEDRAL MICAS BY POLARIZED EXAFS - COMPARISON WITH NMR RESULTS, Physics and Chemistry of Minerals, 17 (1990) 363-370.
[28] B. Ravel, M. Newville, ATHENA, ARTEMIS, HEPHAESTUS: data analysis for X-ray absorption spectroscopy using IFEFFIT, Journal of Synchrotron Radiation, 12 (2005) 537-541.
[29] A. Manceau, D. Chateigner, W.P. Gates, Polarized EXAFS, distance-valence least-squares modeling (DVLS), and quantitative texture analysis approaches to the structural refinement of Garfield nontronite, Physics and Chemistry of Minerals, 25 (1998) 347-365.
[30] J.E. Post, V.F. Buchwald, CRYSTAL-STRUCTURE REFINEMENT OF AKAGANEITE, American Mineralogist, 76 (1991) 272-277.
[31] J. van der Lee, L. De Windt, V. Lagneau, P. Goblet, Module-oriented modeling of reactive transport with HYTEC, Computers & Geosciences, 29 (2003) 265-275.
[32] E. Giffaut, M. Grive, P. Blanc, P. Vieillard, E. Colas, H. Gailhanou, S. Gaboreau, N. Marty, B. Made, L. Duro, Andra thermodynamic database for performance assessment: ThermoChimie, Applied Geochemistry, 49 (2014) 225-236.
[33] S. Szenknect, A. Mesbah, T. Cordara, N. Clavier, H.P. Brau, X. Le Goff, C. Poinssot, R.C. Ewing, N. Dacheux, First experimental determination of the solubility constant of coffinite, Geochimica Et Cosmochimica Acta, 181 (2016) 36-53.
[34] V. Neck, J.I. Kim, Solubility and hydrolysis of tetravalent actinides, Radiochimica Acta, 89 (2001) 1-16.

[35] D.L.A. deFaria, S.V. Silva, M.T. deOliveira, Raman microspectroscopy of some iron oxides and oxyhydroxides, Journal of Raman Spectroscopy, 28 (1997) 873-878.
[36] J. Monnier, D. Neff, S. Reguer, P. Dillmann, L. Bellot-Gurlet, E. Leroy, E. Foy, L. Legrand, I. Guillot, A corrosion study of the ferrous medieval reinforcement of the Amiens cathedral. Phase characterisation and localisation by various microprobes techniques, Corrosion Science, 52 (2010) 695-710.
[37] M.L. Schlegel, F. Martin, M. Fenart, C. Blanc, J. Varlet, E. Foy, D. Pret, N. Trcera, Corrosion at the carbon steel-clay compact interface at 90 degrees C: Insight into short- and long-term corrosion aspects, Corrosion Science, 152 (2019) 31-44.
[38] M.L. Schlegel, S. Necib, S. Daumas, C. Blanc, E. Foy, N. Trcera, A. Romaine, Microstructural characterization of carbon steel corrosion in clay borehole water under anoxic and transient acidic conditions, Corrosion Science, 109 (2016) 126-144.
[39] O. Bildstein, F. Claret, P. Frugier, RTM for Waste Repositories, in: J.L. Druhan, C. Tournassat (Eds.) Reactive Transport in Natural and Engineered Systems, 2019, pp. 419-457.
[40] M. Wilke, F. Farges, P.E. Petit, G.E. Brown, F. Martin, Oxidation state and coordination of Fe in minerals: An FeK-XANES spectroscopic study, American Mineralogist, 86 (2001) 714-730.
[41] T.E. Westre, P. Kennepohl, J.G. DeWitt, B. Hedman, K.O. Hodgson, E.I. Solomon, A multiplet analysis of Fe K-edge 1s->3d pre-edge features of iron complexes, Journal of the American Chemical Society, 119 (1997) 6297-6314.
[42] J.M. Cerrato, C.J. Barrows, L.Y. Blue, J.S. Lezama-Pacheco, J.R. Bargar, D.E. Giammar, Effect of Ca2+ and Zn2+ on UO2 Dissolution Rates, Environmental Science & Technology, 46 (2012) 2731-2737.
[43] B.G. Santos, J.J. Noel, D.W. Shoesmith, b, The influence of silicate on the development of acidity in corrosion product deposits on SIMFUEL (UO2), Corrosion Science, 48 (2006) 3852-3868.
[44] B.G. Santos, J.J. Noel, D.W. Shoesmith, a, The influence of calcium ions on the development of acidity in corrosion product deposits on SIMFUEL, UO2, Journal of Nuclear Materials, 350 (2006) 320-331.
[45] C.N. Wilson, W.J. Gray, MEASUREMENT OF SOLUBLE NUCLIDE DISSOLUTION RATES FROM SPENT FUEL, 1990.
[46] D.Q. Cui, K. Spahiu, P. Wersin, Redox reactions of iron and uranium dioxide in simulated cement pore water under anoxic conditions, in: R.J. Finch, D.B. Bullen (Eds.) Scientific Basis for Nuclear Waste Management Xxvi, 2003, pp. 427-432.
[47] P.C. Burns, R.C. Ewing, A. Navrotsky, Nuclear Fuel in a Reactor Accident, Science, 335 (2012) 1184-1188.
[48] F.M.S. Maia, S. Ribet, C. Bailly, M. Grive, B. Made, G. Montavon, Evaluation of thermodynamic data for aqueous Ca-U(VI)-CO3 species under conditions characteristic of geological clay formation, Applied Geochemistry, 124 (2021).
[49] S. Szenknect, D. Alby, M.L. Garcia, C.X. Wang, R. Podor, F. Miserque, A. Mesbah, L. Duro, L.Z. Evins, N. Dacheux, J. Bruno, R.C. Ewing, Coffinite formation from UO2+x, Scientific Reports, 10 (2020).
[50] A. Espriu-Gascon, D.W. Shoesmith, J. Gimenez, I. Casas, J. de Pablo, Study of SIMFUEL corrosion under hyper-alkaline conditions in the presence of silicate and calcium, Mrs Advances, 2 (2017) 543-548.
[51] M.E. Broczkowski, J.J. Noel, D.W. Shoesmith, The inhibiting effects of hydrogen on the corrosion of uranium dioxide under nuclear waste disposal conditions, Journal of Nuclear Materials, 346 (2005) 16-23.
[52] P. Carbol, P. Fors, T. Gouder, K. Spahlu, Hydrogen suppresses UO2 corrosion, Geochimica Et Cosmochimica Acta, 73 (2009) 4366-4375.
[53] B. Muzeau, C. Jegou, F. Delaunay, V. Broudic, A. Brevet, H. Catalette, E. Simoni, C. Corbel, Radiolytic oxidation of UO2 pellets doped with alpha-emitters (Pu-238/239), Journal of Alloys and Compounds, 467 (2009) 578-589.

[54] D. Cui, J. Low, C.J. Sjostedt, K. Spahiu, On Mo-Ru-Tc-Pd-Rh-Te alloy particles extracted from spent fuel and their leaching behavior under Ar and H-2 atmospheres, Radiochimica Acta, 92 (2004) 551-555.
[55] C.A. Colmenares, OXIDATION MECHANISMS AND CATALYTIC PROPERTIES OF THE ACTINIDES, Progress in Solid State Chemistry, 15 (1984) 257-364.
[56] H. Christensen, S. Sunder, An evaluation of water layer thickness effective in the oxidation of UO2 fuel due to radiolysis of water, Journal of Nuclear Materials, 238 (1996) 70-77.
[57] M. Amme, W. Bors, C. Michel, K. Stettmaier, G. Rasmussen, M. Betti, Effects of Fe(II) and hydrogen peroxide interaction upon dissolving U0(2) under geologic repository conditions, Environmental Science & Technology, 39 (2005) 221-229.
[58] M. Odorowski, Etude de l'altération de la matrice (U,Pu)O2 du combustible irradié en conditions de stockage géologique: approche expérimentale et modélisation géochimique., in: MINES ParisTech, PSL University, Centre de Géosciences, 2015, pp. Ph.D. Thesis, 277 pages.
[59] D.Q. Cui, K. Spahiu, The reduction of U(VI) on corroded iron under anoxic conditions, Radiochimica Acta, 90 (2002) 623-628.
[60] B.T. Tan, A.J. Popel, R.J. Wilbraham, J. Day, G.I. Lampronti, C. Boxall, I. Farnan, Surface and electrochemical controls on UO2 dissolution under anoxic conditions, Journal of Nuclear Materials, 520 (2019) 41-55.
[61] D.E. Latta, B. Mishra, R.E. Cook, K.M. Kemner, M.I. Boyanov, Stable U(IV) Complexes Form at High-Affinity Mineral Surface Sites, Environmental Science & Technology, 48 (2014) 1683-1691.
[62] H. Christensen, E. Bjergbakke, Application of chemsimul for groundwater radiolysis, Nuclear and Chemical Waste Management, 6 (1986) 265-270.
[63] V. Kerleguer, C. Jegou, L. De Windt, V. Broudic, G. Jouan, S. Miro, F. Tocino, C. Martin, The mechanisms of alteration of a homogeneous U0.73PU0.27O2 MOx fuel under alpha radiolysis of water, Journal of Nuclear Materials, 529 (2020).

List of Figures

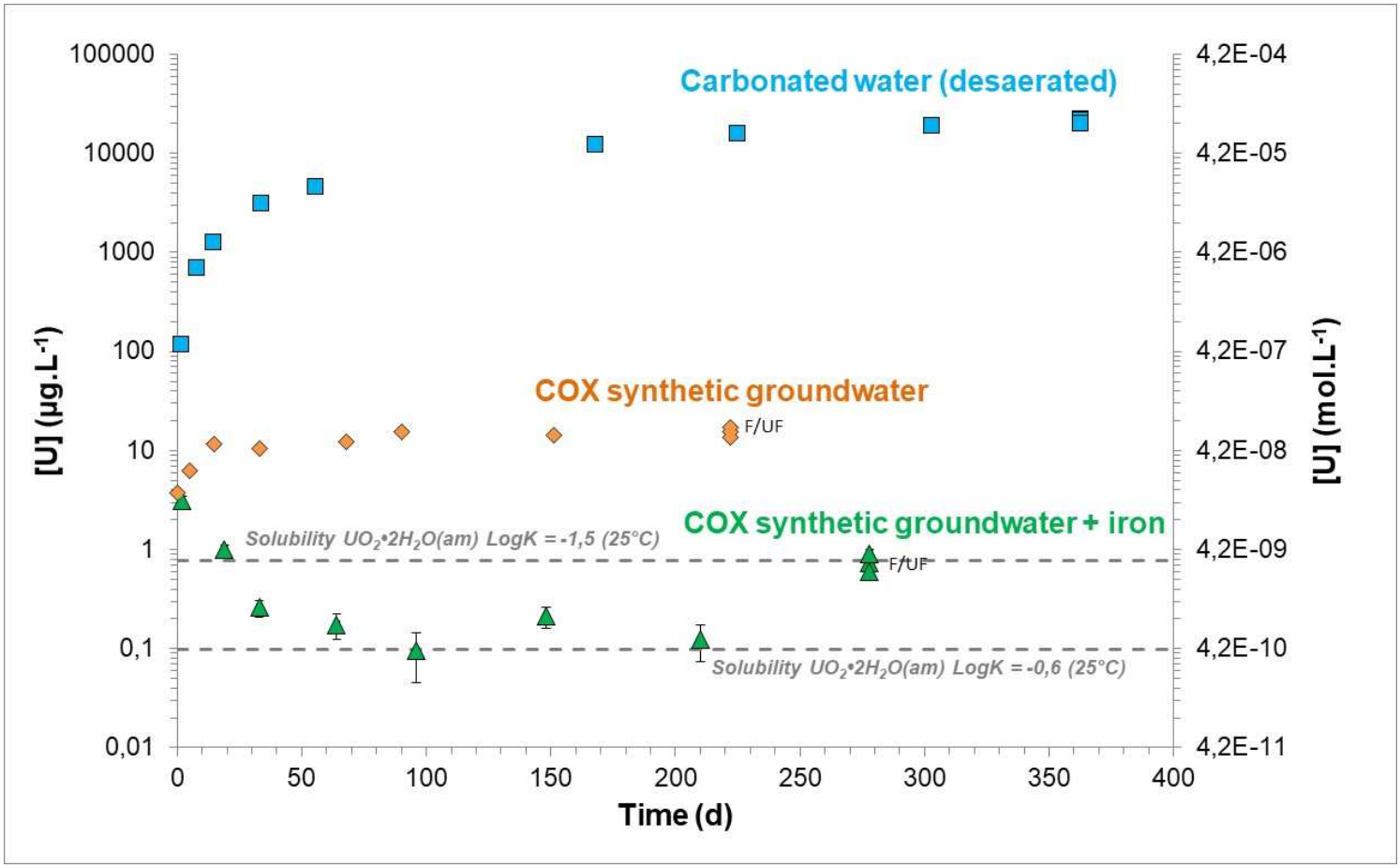

Figure 1: Evolution of uranium concentrations in solution during leaching of MOX Mimas pellets in different environments. F: filtered sample. UF: ultra-filtered sample. The dashed lines stand for the solubility limits of the amorphous $UO_2.xH_2O$ found in the literature (Sec. 2.1).

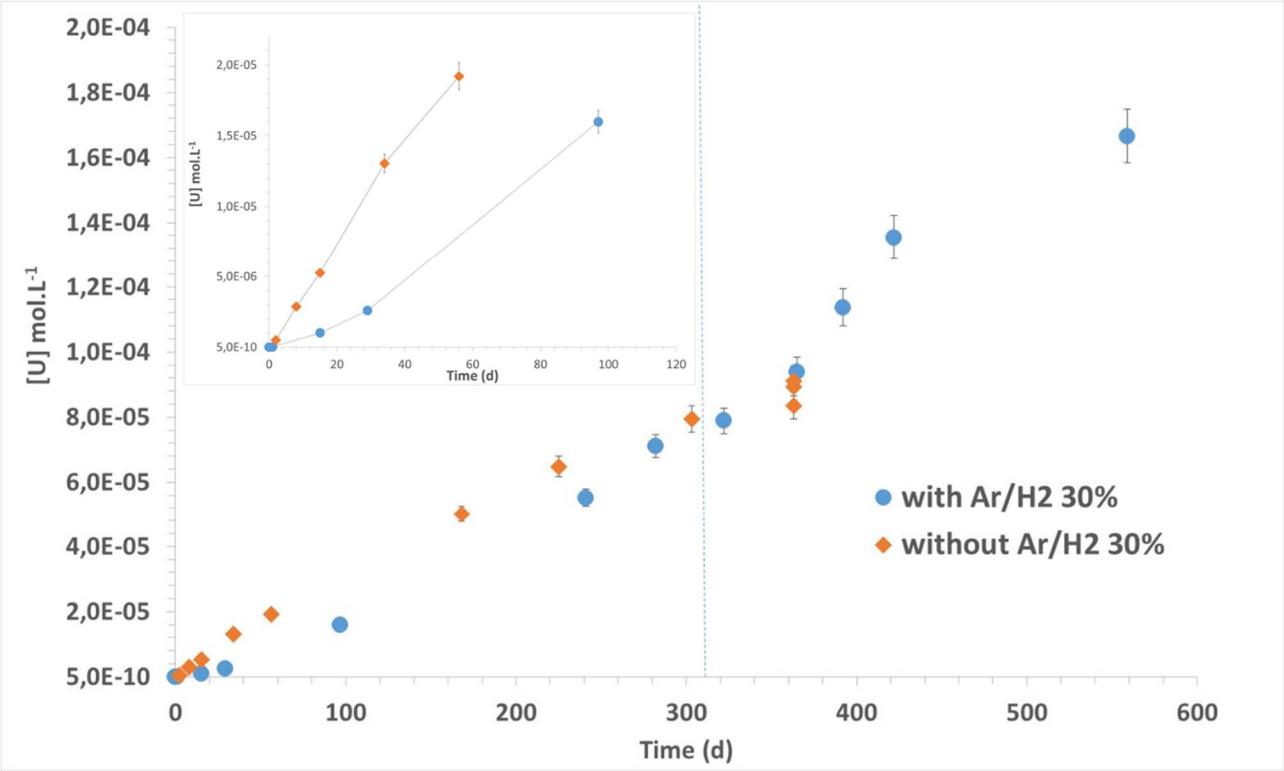

Figure 2: Evolution of uranium concentrations in solution during leaching of MOX Mimas pellets in a carbonated water (10^{-2} M), with and without hydrogen (3.5 bars Ar/H_2 70/30% up to 322 days, then 5 bars up to 559 days). The box at the top left shows the concentration evolutions during the first days of leaching.

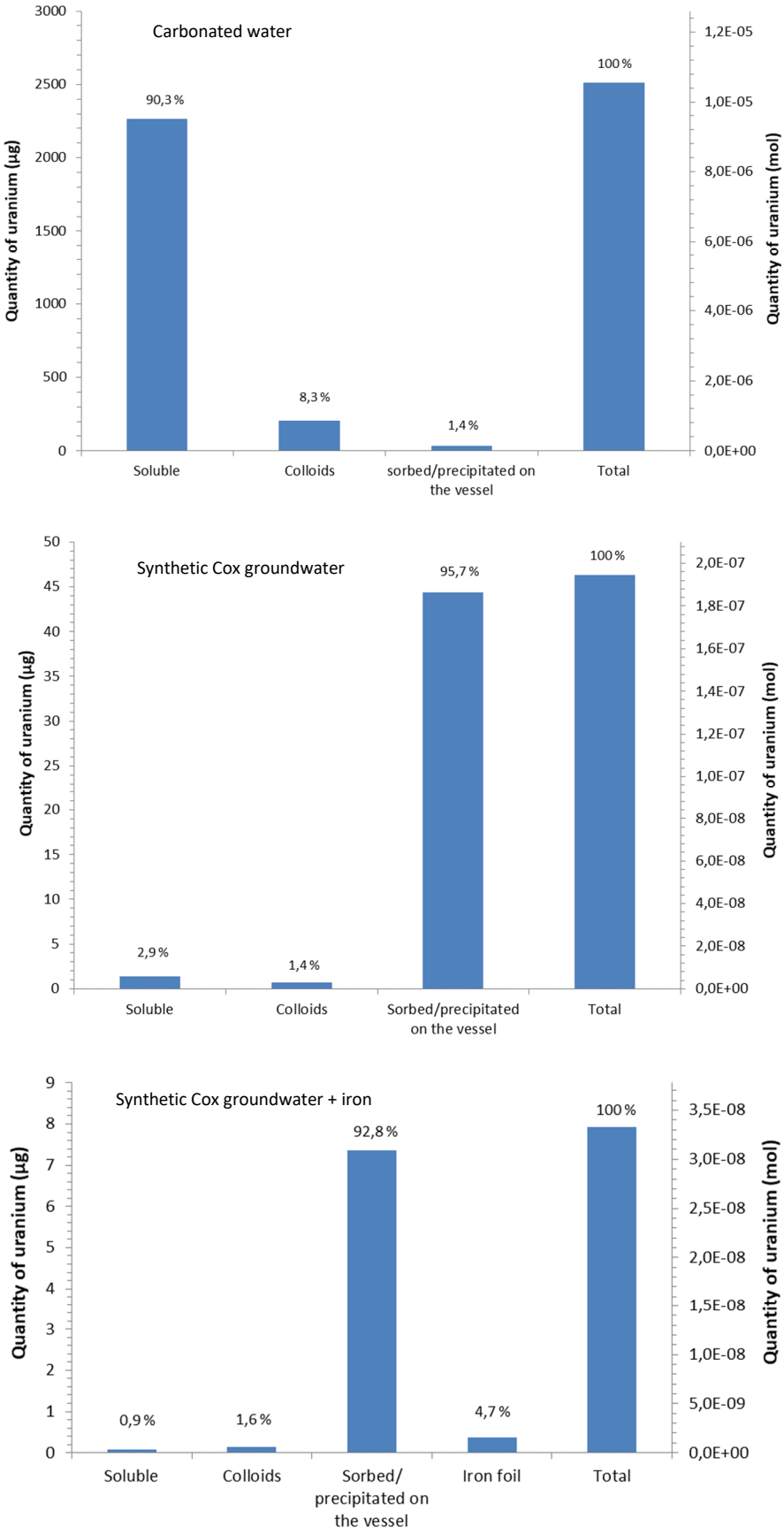

Figure 3: Uranium distribution among the solution, the colloids, and the sorbed/precipitated fraction on the TiO_2 walls or the iron foil at the end of the MOX leaching experiments.

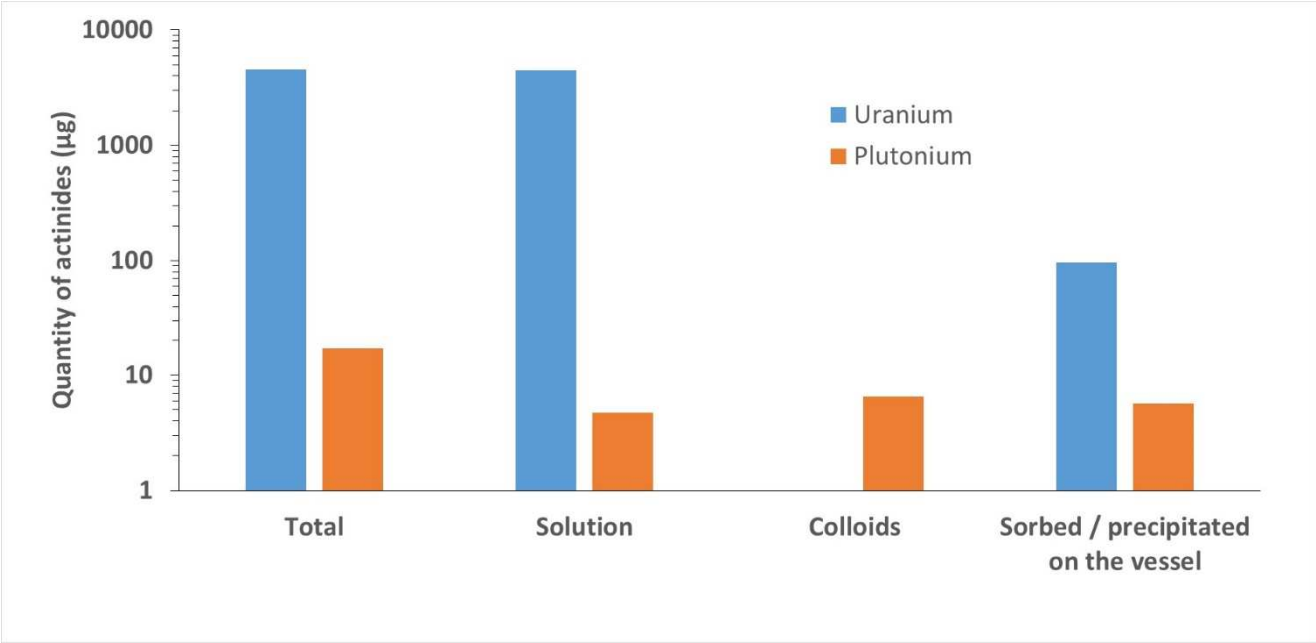

Figure 4: Uranium and plutonium distributions among the solution, the colloids, and the sorbed/precipitated fraction on the TiO_2 walls at the end (559 days) of the MOX Mimas leaching experiment in carbonated water (10^{-2} M), with H_2 (3.5 bars Ar/H_2 70/30% up to 322 days, then 5 bars up to 559 days).

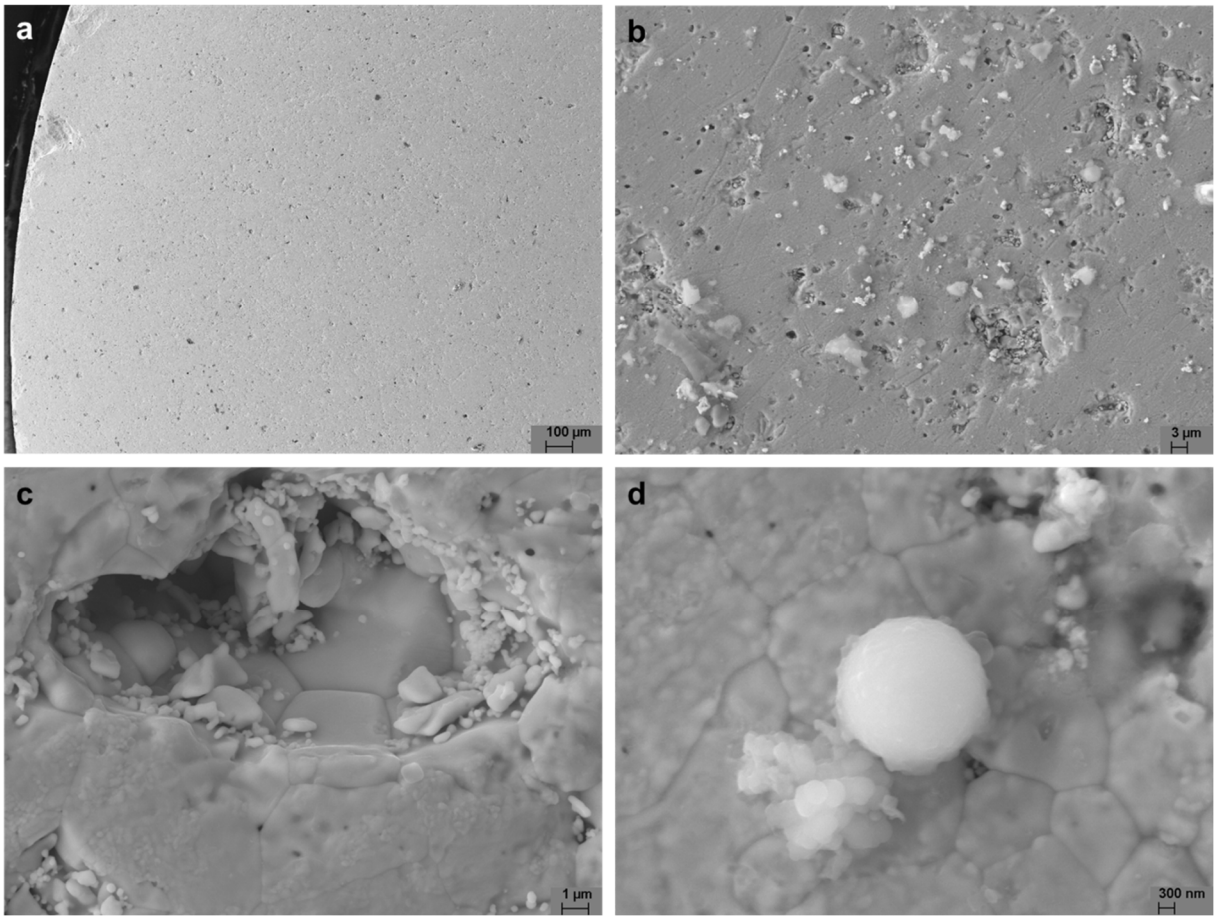

Figure 5: SEM micrographs of the surface of a Mimas MOX pellet (7.48 wt.%) altered in synthetic Cox groundwater. The surface does not show a significant precipitation of secondary covering phases at a μm^3 scale. Nevertheless, nodules containing silicium and potentially uranium can be observed.

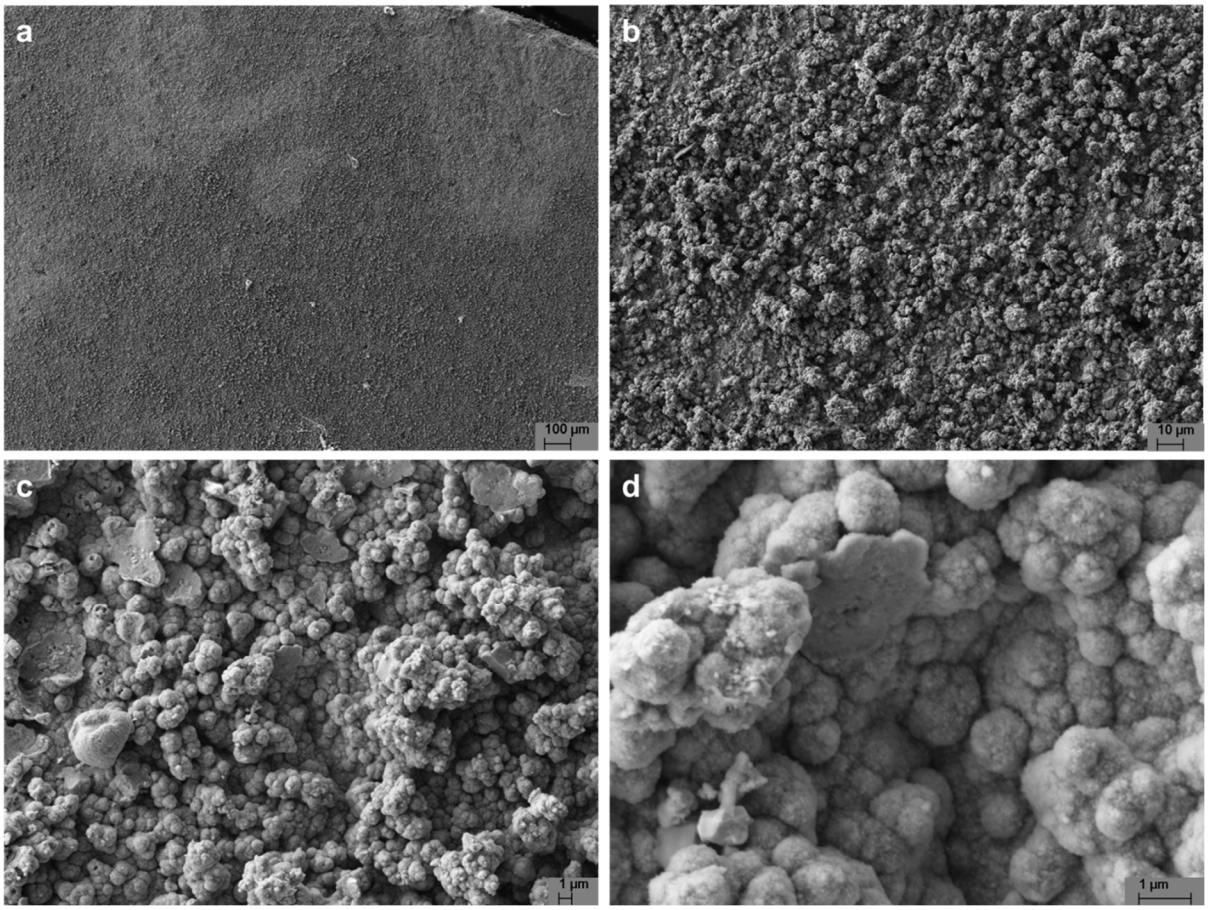

Figure 6: SEM micrographs of the surface of a Mimas MOX pellet (7.48 wt.%) altered in synthetic Cox groundwater in the presence of metallic iron. The MOX pellet surface is completely covered with an iron precipitate.

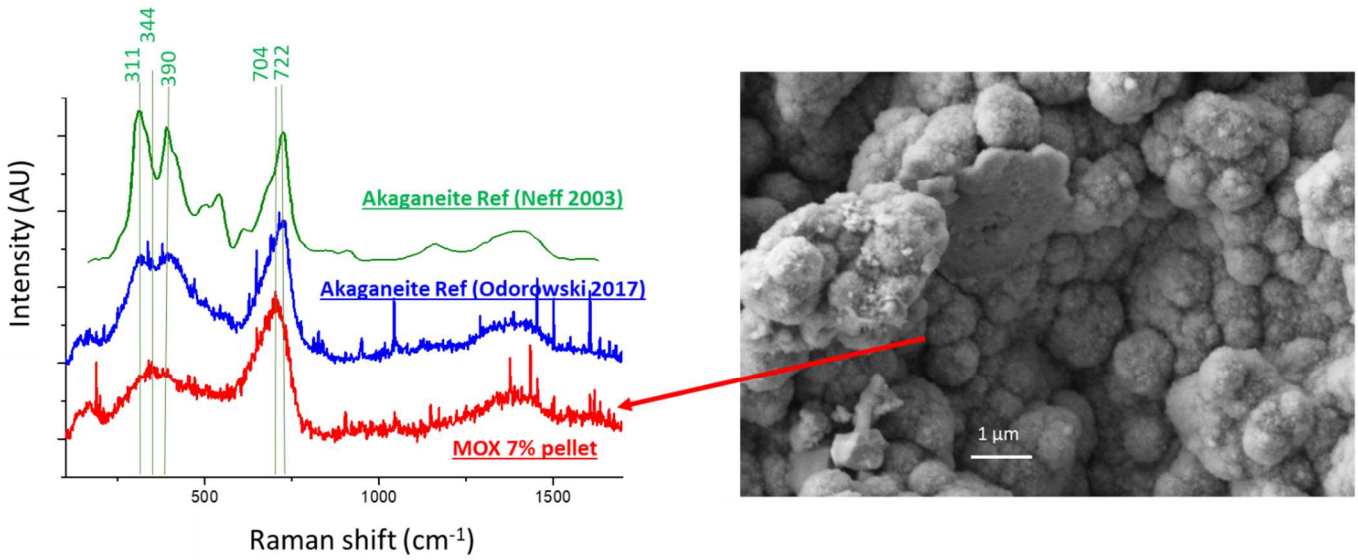

Figure 7: Raman spectrum (red) of precipitates found on the Mimas MOX pellets (7.48 wt.%) leached in synthetic Cox groundwater in the presence of metallic iron, and comparison with literature data (green: Neff, 2003 and blue: Odorowski, 2017).

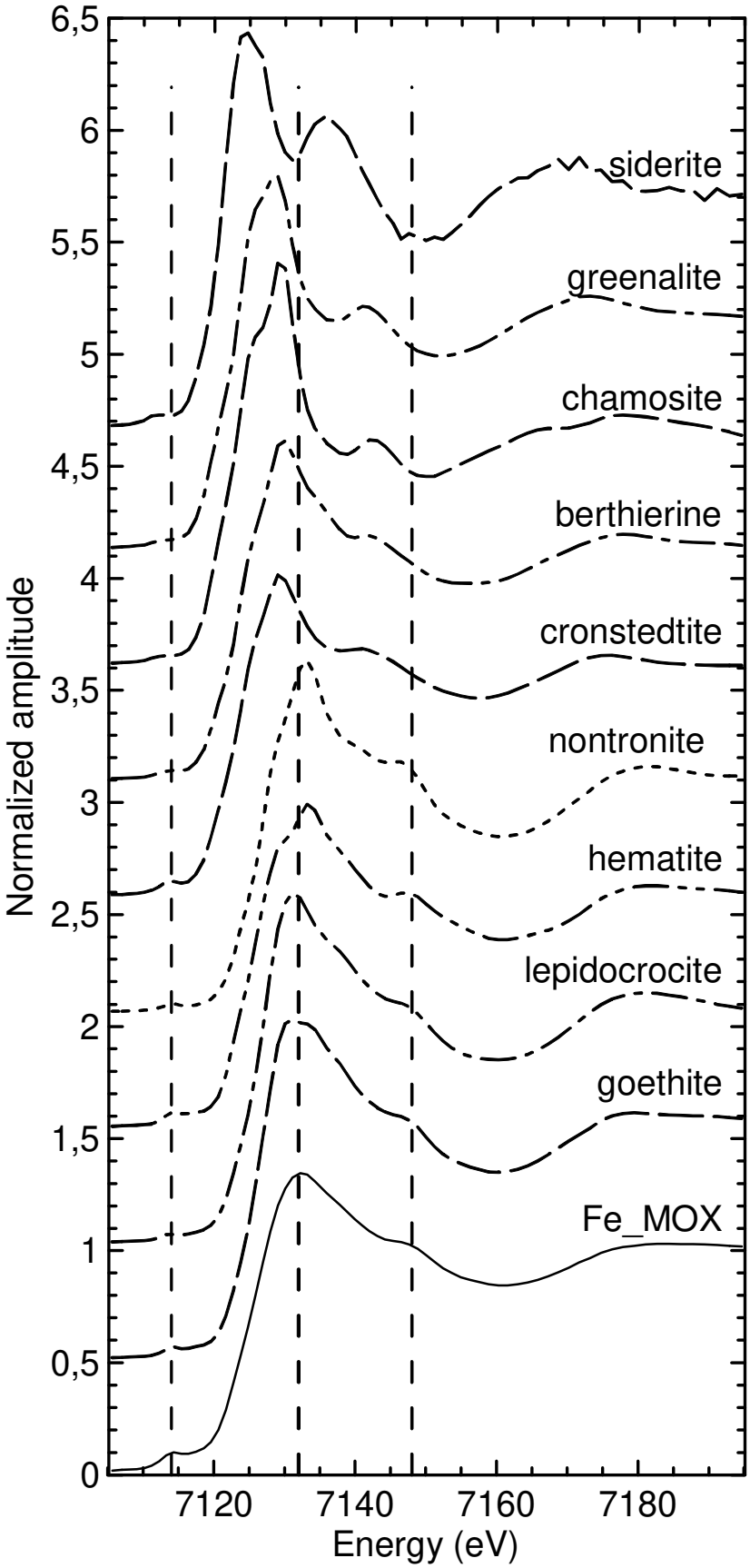

Figure 8: Comparison of XANES spectra for the reference Fe and the Fe_MOX samples. Spectra are offset for clarity.

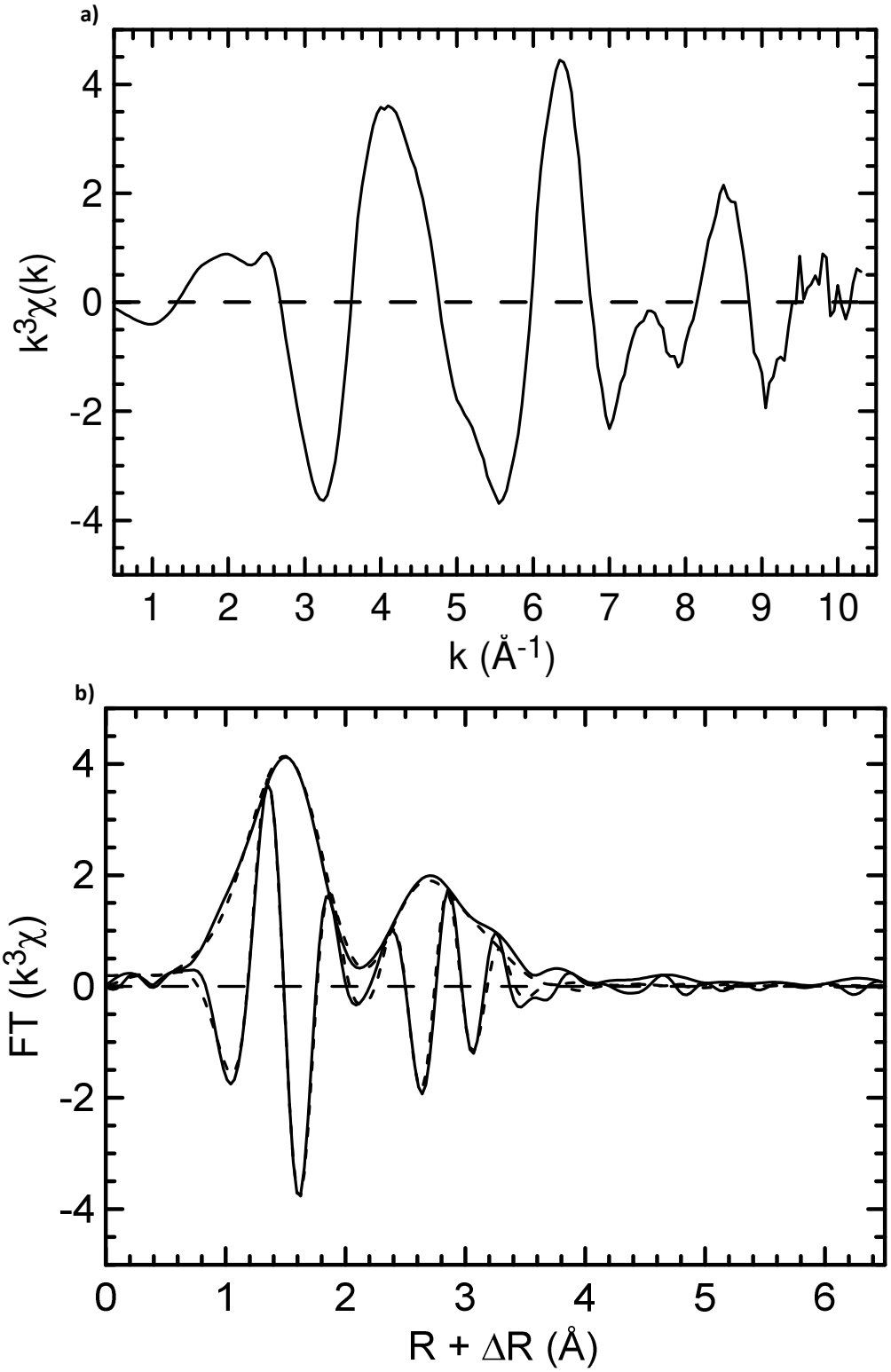

Figure 9: **a)** EXAFS spectrum for Fe in the corrosion products on the MOX pellet. **b)** FT (solid lines) and best-fit (dashed line) for EXAFS data of Fe in the corrosion products on the MOX pellet.

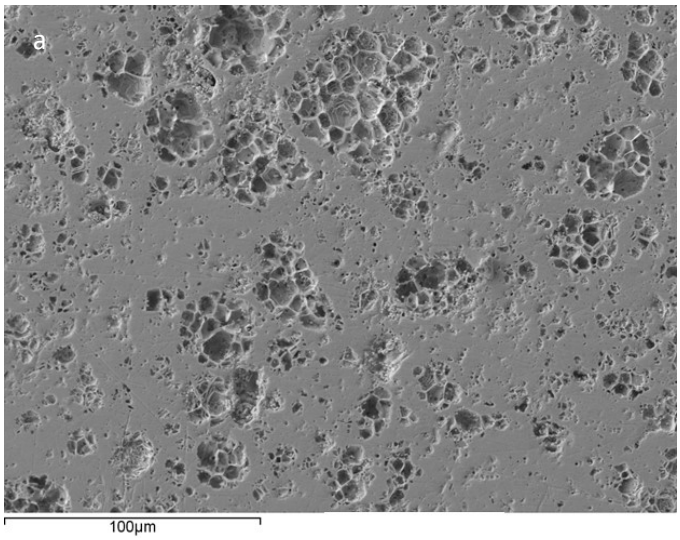

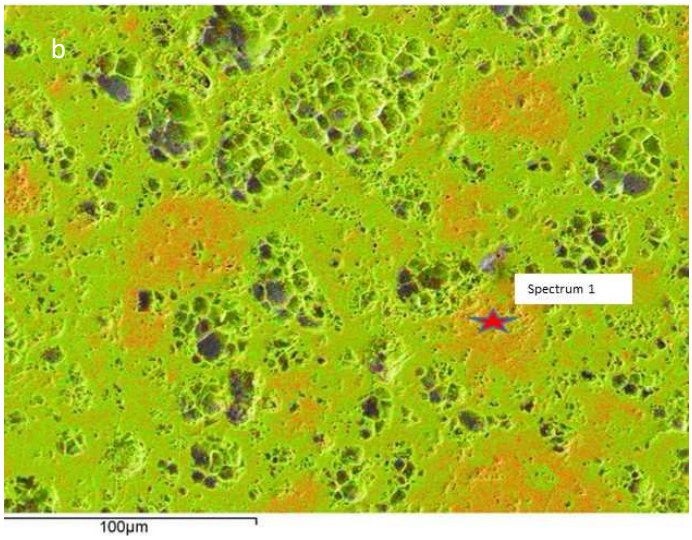

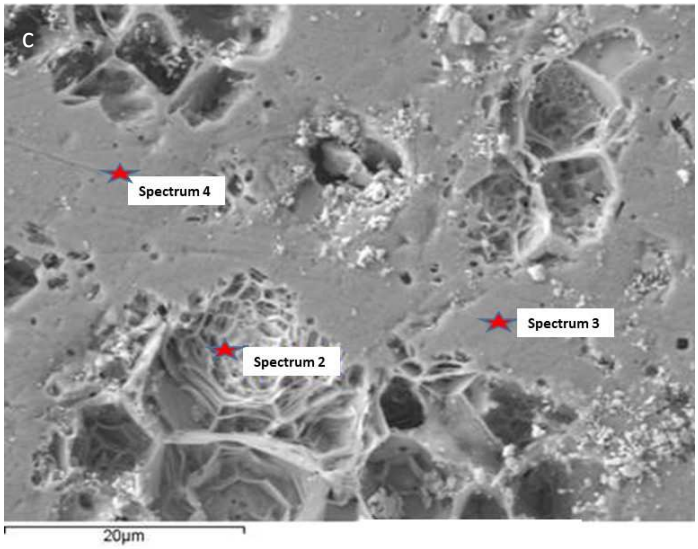

Actinides	Spectrum 1 wt% and at%	Spectrum 2 wt% and at%
U (M)	71.51 – 72.01	98.28 - 98.32
Pu (M)	28.49 – 27.99	1.72 - 1.68
Total	100	100

Actinides	Spectrum 3 wt% and at%	Spectrum 4 wt% and at%
U (M)	89.06 – 89.29	89.30 – 89.54
Pu (M)	10.94 – 10.71	10.70 – 10.46
Total	100	100

Figure 10: SEM micrographs and EDX analyses of MOX Mimas pellets (7.48 wt.%) leached in a carbonated water (10^{-2} M) with hydrogen (3.5 bars Ar/H_2 70/30% up to 322 days, then 5 bars up to 559 days). The surface shows corrosion pits corresponding to the areas with a low plutonium content (< 2 wt.%). The red zones correspond to plutonium-enriched aggregates.

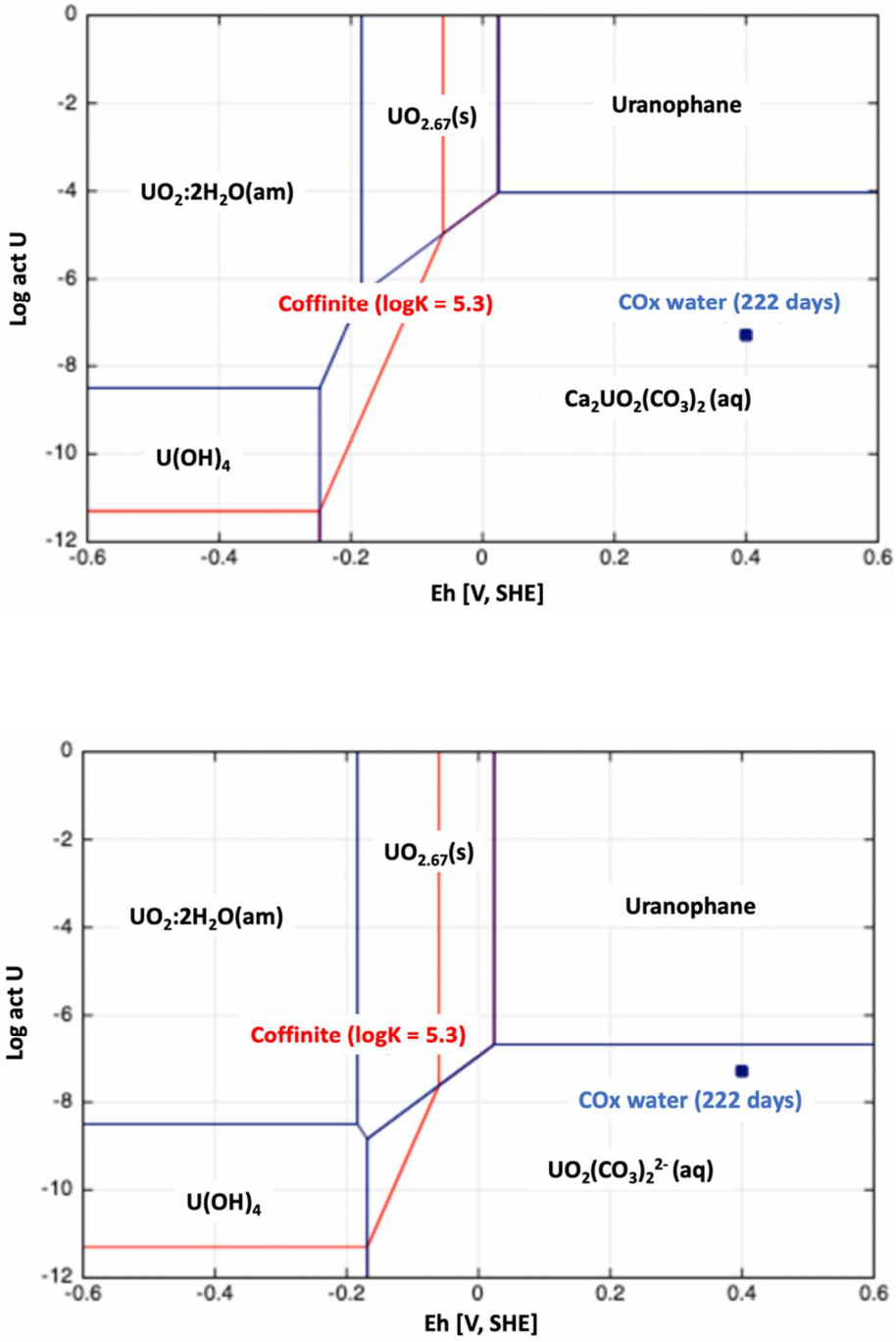

Figure 11: Solubility diagrams of uranium as a function of redox potential, with (top) and without (bottom) the ternary complexes $Ca_2UO_2(CO_3)_3$ and $CaUO_2(CO_3)_3^{2-}$ calculated with the Thermochimie database [32] except for coffinite [33] (Sec. 1.4). The diagrams were plotted for a temperature of 25°C, pH = 7.1, activity HCO_3^- = 1×10^{-3} (with ternary complexes) or 2×10^{-3} (no ternary complexes), activity H_4SiO_4 = 1×10^{-4}, and activity Ca^{2+} = 5×10^{-3}.

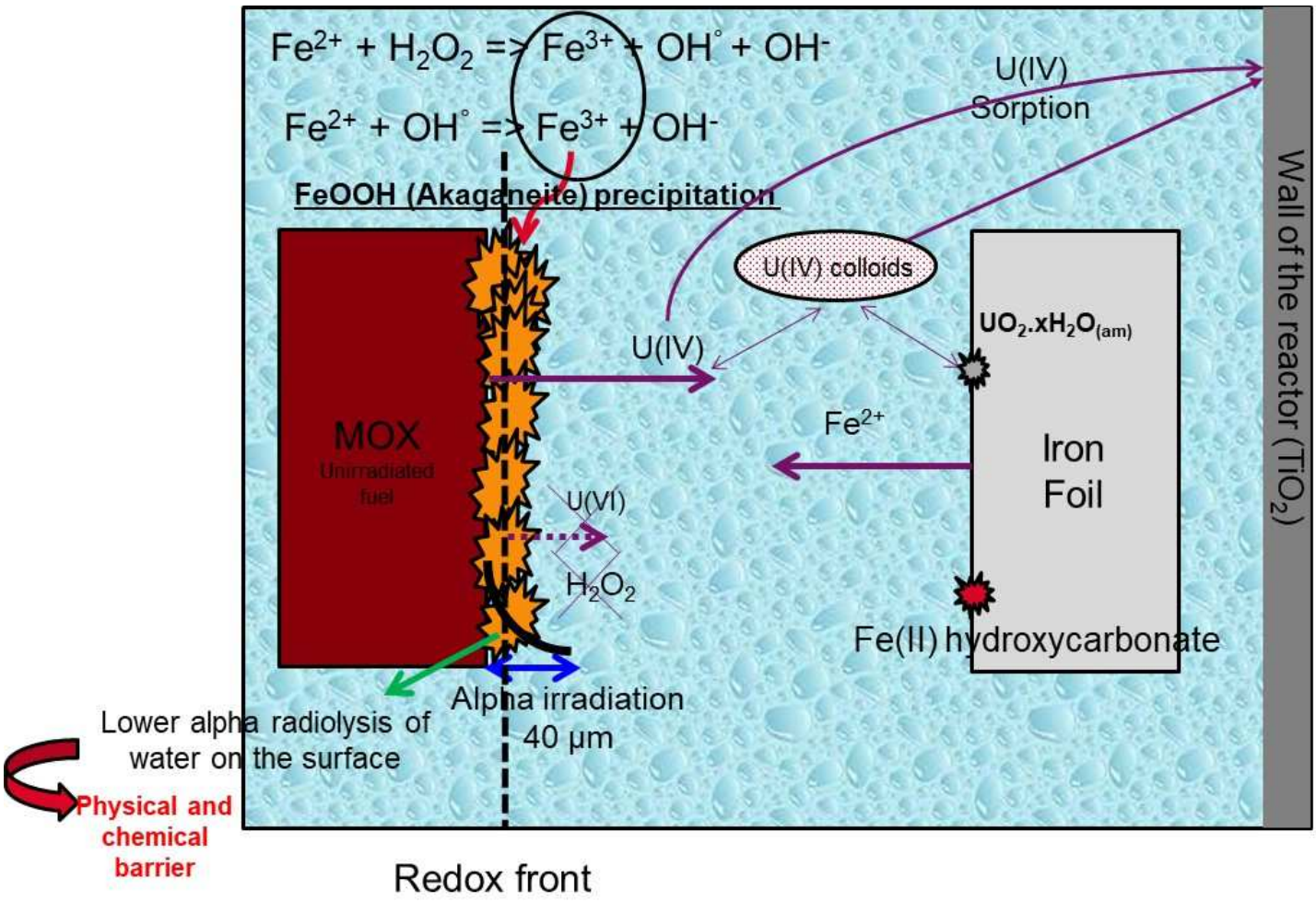

Figure 12: Mimas MOX fuel alteration mechanisms in synthetic Cox groundwater in the presence of metallic iron (corroded foil).

List of tables

Oxide composition (wt %)		Isotopic composition (wt %) June 2000					
UO_2	PuO_2	^{238}Pu	^{239}Pu	^{240}Pu	^{241}Pu	^{242}Pu	^{241}Am
92.52	7.48	1.72	58.06	25.51	6.80	6.19	1.72

Table 1: Isotopic composition of the Mimas MOX non-irradiated fuel pellets.

Solution	Atmosphere	Other material	Leaching duration
Carbonated water	Argon	-	363 days
Carbonated water	Ar/H_2 (70/30%)	-	559 days
Synthetic COx water	Ar/CO_2 3000 ppm	-	222 days
Synthetic COx water	Ar/CO_2 3000 ppm	Iron foil	278 days

Table 2: Characteristics of the leaching tests performed with the Mimas MOX fuel pellets.

Time (d)	0	1	15	29	97	241	282	322
P_{total} (bars)	3.50	3.40	3.30	3.20	3.10	3.05	2.95	2.90
% H_2 (μ-GC_{meas})	29.57							27.46
$[H_2]_{sol}$ mol.L^{-1}	$8.18x10^{-4}$							$6.29x10^{-4}$

Time (d)	322	365	392	422	559
P_{total} (bars)	5.0	4.90	4.80	4.70	4.60
% H_2 (μ-GC_{meas})	28.98				
$[H_2]_{sol}$ mol.L^{-1}	$1.20x10^{-3}$				

Table 3: Evolution of the total pressure in the reactor and hydrogen content measurements in the gas phase: at the start of the experiment, after 322 days of leaching just before the increase to 5 bars, and just after the change. The calculated amount of dissolved hydrogen in the water is based on Henry's law constant at 25°C.

	$[Na^+]$	$[K^+]$	$[Ca^{2+}]$	$[Mg^{2+}]$	$[Sr^{2+}]$	$[Cl^-]$	$[SO_4^{2-}]$	$[HCO_3^-]$	[Si]
mg.L^{-1}	993	39.1	341	131	17.5	1454	1412	146	5.62
mol.L^{-1}	0.0432	0.0010	0.0085	0.0054	0.0002	0.0410	0.0147	0.0024	0.0002

Table 4: Chemical composition of the synthetic Callovian-Oxfordian claystone water at 25°C.

Shell	Structural parameters		
	N	R (Å)	σ (Å)
O	3.1(8)	1.92	0.062(16)
O	3.0(8)	2.06	0.062(16)
Fe	1.6(5)	3.01	0.009(2)
Fe	1.8(7)	3.46	0.009(2)
O	2.5(2.0)	4.20(13)	0.009[f]

F value held fixed during the fitting procedure.

Table 5: Best fit results for the modelling of the EXAFS spectrum for Fe in the MOX corrosion products. ΔE_0 = -0.1 V. reduced chi-square 174. R factor 0.0166.

U(VI) minerals	Saturation indexes	
	with ternary complexes	without ternary complexes
Hydroxides		
schoepite	-6.6	-4.6
Silicates		
soddyite(synt1)	-8.9	-4.9
soddyite(synt2)	-11.4	-7.4
uranophane	-6.5	-2.5
Others		
becquerelite(nat)	-21.3	-9.0
rutherfordine	-6.1	-4.1

Table 6: Saturation index calculations (CHESS, database: Thermochimie v9) at 25°C, calculated with and without the ternary complexes $Ca_2UO_2(CO_3)_3$ and $Ca_2UO_2(CO_3)_3^{2-}$; $[U]_{tot}$= 5x10^{-8} mol.L^{-1}, pH = 7.1, and the full chemical composition of the synthetic Callovian-Oxfordian claystone water (Table 2).

Calculation point from the surface	γ dose rates (mGy.h^{-1})	β dose rates (mGy.h^{-1})
50 µm	183.79	1.37
100 µm	172.73	1.29
1 cm	2.03	0
2 cm	0.57	0
3 cm	0.25	0
4 cm	0.13	0
5 cm	0.08	0
6 cm	0.05	0
7 cm	0.03	0
8 cm	0.02	0

Table 7: Evolution of the γ and β dose rates from the MOX pellet surface, calculated using the calculation codes MCNP® 5.0 (γ dose rates) and VARSKIN® 3.1.0 (β dose rates).